Technobius Physics

A peer-reviewed open-access journal

CONTENTS
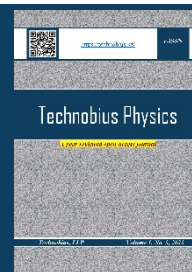
Exploring particle physics through diffusion chambers: detecting, visualizing, and analyzing subatomic phenomena

Dastan Zhumanov[1,*], Cholpon Maripova[2]

[1]Institute of Automation and Information Technologies, Satbayev University, 22a Satpaev Str., Almaty, Kazakhstan
[2]Department of Physics, Kyrgyz State Technical University, 66, Ch.Aitmatov Ave., Bishkek, Kyrgyzstan
*Correspondence: dastan.zhumanov.02@mail.ru

Abstract. This study examines the development and utilization of diffusion chambers in particle physics research. Through meticulous experimentation, optimization of chamber parameters has been achieved to enhance particle detection while concurrently assessing background radiation levels, vital for minimizing interference. Furthermore, recent advancements have enabled the visualization of α – particles and mesons within these chambers, offering invaluable insights into their behaviors and interactions. These achievements highlight the pivotal role of diffusion chambers as indispensable tools in advancing our understanding of fundamental particles and their properties. As a result, diffusion chambers continue to serve as critical instruments in unraveling the mysteries of the subatomic world, promising continued contributions to particle physics research.
Keywords: diffusion chambers, particle physics, background radiation, α – particles, mesons.

1. Introduction

1.1 Cosmic radiation

High intensity particle radiations (photon rays being an example, since they are electromagnetic waves) usually come from space and penetrate all layers of the Earth's atmosphere (called main cosmic radiations). These radiations' principal constituents are as follows: protons (approx. 90%), α – particles (approx. 9%), bigger nuclei (up to 1%) [1].

Particles often clash with atmospheric nuclei as they pass through the atmosphere, starting fission and nuclear reactions. As a result, fresh nuclei and fundamental particles are created, continuing on their current path and triggering other interactions [2].

There is only one detectable secondary form of radiation in the atmospheric layers closest to the Earth's surface (below 20 km), which originates from the many interaction processes occurring in the upper atmospheric layers [3].

It thus becomes necessary to differentiate between four different parts, each with a different penetration strength. Table 1 gives information on the detailed composition of the components [2], [3], [4].

Table 1 – Components of the cosmic secondary rays

Cosmic secondary rays	Components
Nucleons	Protons / neutrons
Electrons and photons	Electrons / positrons / photons
Mesons	Mesons of different charges
Neutrinos	Neutrinos / antineutrinos

Figure 1 schematically illustrate the expansion process of secondary cosmic ray components.
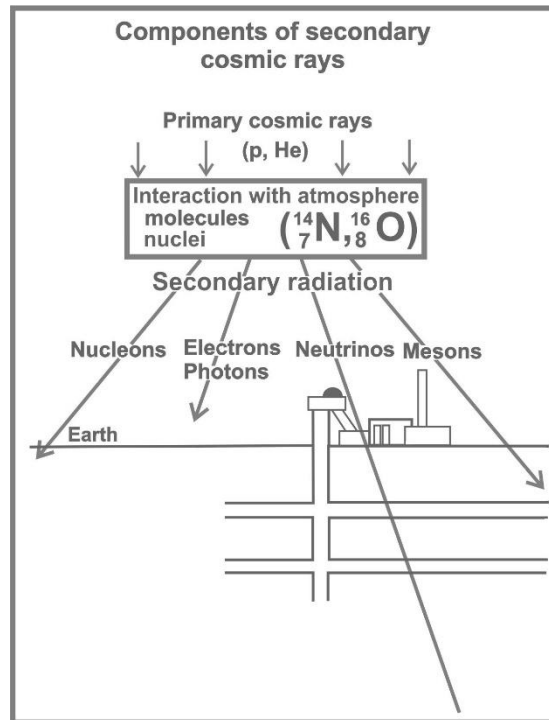
Figure 1 – Organic division mechanisms

All electrically charged particles, such as protons, electrons, positrons, mesons, and alpha particles, can be found inside the special equipment [5]. On the other hand, photons only produce an indirect trace when they, for example, remove an electron from an atom, leaving behind an ionization trail. Because neutrons can initiate nuclear reactions, they cause traces to be formed through the charged particles that are released from the nucleus. Table 2 summarizes the components of the trace that is left behind by the nuclear reactions of neutrons [6].

Table 2 – The trace that is left behind by the nuclear reactions of neutrons

Particles	Symbol	Relative mass	Charge	Radioactive period
Electron	e^-	1	-1	Stable
Positron	e^+	1	+1	Stable
Myon	μ^-	206.77	-1	$1.5 * 10^{-6}$ s
Antimyon	μ^+	206.77	+1	$1.5 * 10^{-6}$ s
Proton	p^+	1836.1	+1	stable
Neutron	n	1836.62	0	14.7 min
α – particle	He^{++}	7294.1	+2	Stable

1.2 Radiations from the earth (Terrestrial)

Natural radionuclides that emit radiation are present in all elements on Earth, including the atmosphere, water, animals, and soil [7], [8]. They have either always existed or have been created since the Earth's creation, which is approximately 4.5 billion years ago: Among the naturally occurring radionuclides are U-238, Th-232, K-40, and Rb-87, which have extremely long radioactive periods [8]. There is a continuous production of Ra-226, Rn-222, Po-218, or Pb-210, radionuclides with relatively short radioactive periods in the three natural splitting processes. Naturally occurring radionuclides with comparatively short radioactive periods do exist, but they are not involved in the splitting process. In the highest layers of the atmosphere, they are continuously being formed. For example, C-14 from N-14 or H-3 from N-14 or O-16.

There are roughly 100 naturally occurring radionuclides in the Earth's crust, all of which exist in varying amounts and have existed since the planet's formation. This explains the continuous exchanges that occur between the atmosphere, water, earth, and animal life (Figure 2).
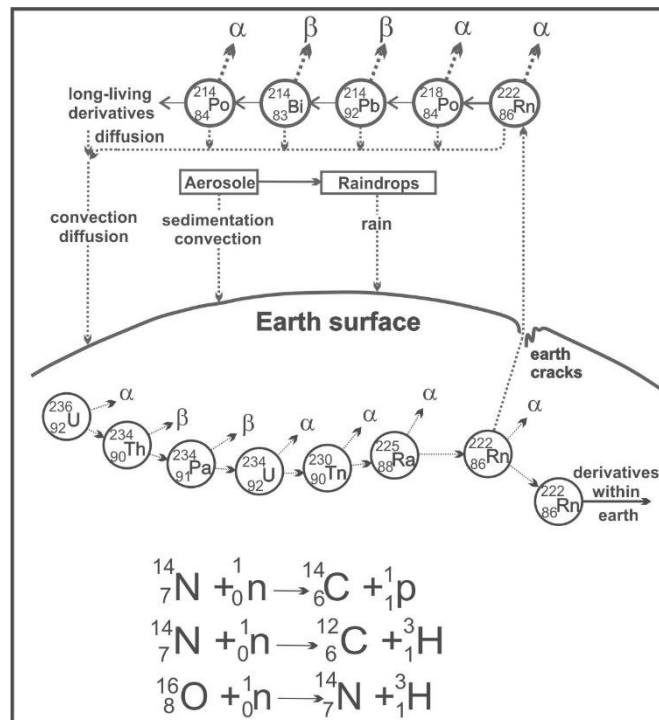
Figure 2 – Production of Rn-222 and derivatives in the low atmosphere layer

As it is known, not a few researches have been carried out in the field of creation of diffusion chambers for observation of charged particle tracks [9]. Some scientists [10] conducted experiments to determine the most suitable materials for making a diffusion chamber. They tested different substances to assess their compatibility with particle track detection and visualisation. Factors such as transparency, durability and sensitivity to ionisation were evaluated. Through systematic testing and comparison, materials such as glass or plastic were identified as having optimal characteristics for use in the chamber, but the sensitivity of the chamber was not ideal.

Other researchers [11] have explored different camera configurations and geometries to improve particle detection and track visualisation. They experimented with camera sizes, shapes and detection element locations to maximise sensitivity and resolution. By systematically changing these parameters and analysing the resulting particle tracks, they were unable to improve the camera design to achieve optimal performance.

The team of scientists [12] conducted extensive research to determine the ideal operating conditions for the diffusion chamber. They adjusted parameters such as temperature, pressure and gas composition to optimise particle detection efficiency and track visibility.

Through systematic experimentation and data analysis, they determined the optimal range of operating parameters that facilitated the most accurate and reliable observation of particle tracks in the chamber.

Consequently, there arises a necessity to devise a chamber constructed from naturally occurring radioactive elements.

2. Methods

A special diffusion chamber was constructed for the experiment, which consisted of a chamber base and an observation chamber, the two main parts of the cloud chamber device. The

camera base includes a pump, a programmable time switch, a power supply, a cooling mechanism and an alcohol reservoir. The surveillance camera is attached to this base. At the bottom of the surveillance camera is a large black metal panel measuring 45 by 45 cm, which is continuously cooled to a temperature of about -30°C using a cooling device (Figure 3).
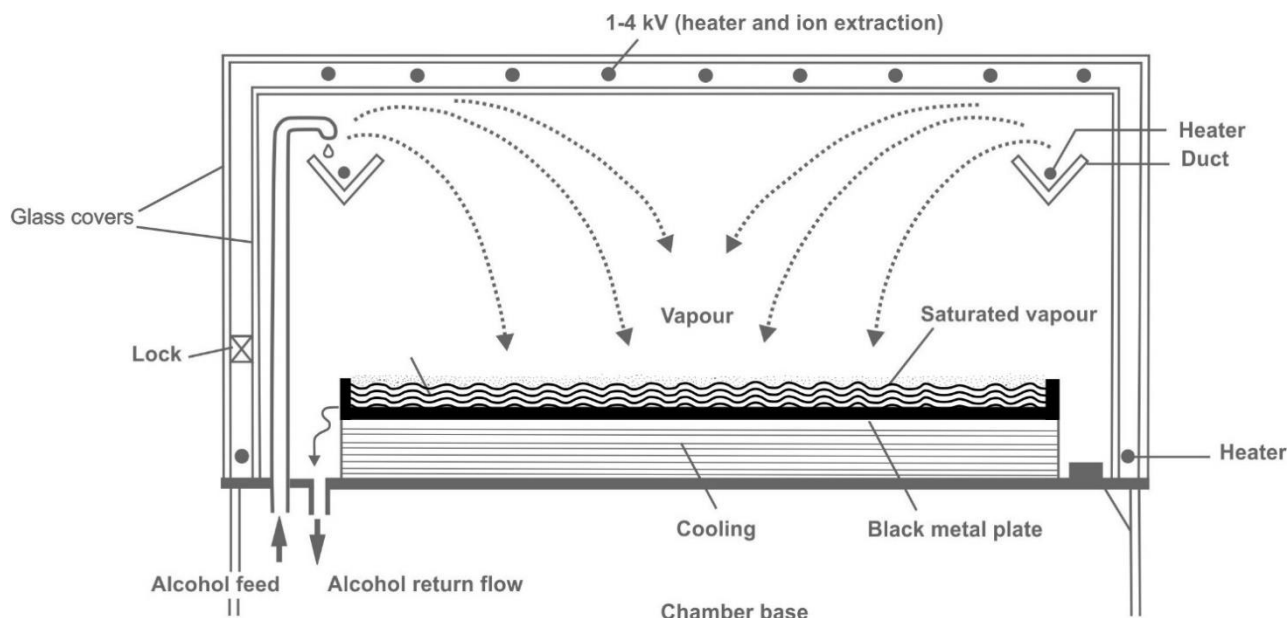
Figure 3 – Segment via the cloud diffusion chamber

The surveillance camera consists of two folded glass covers for the side and top plates. A system of tiny heating wires is located inside this structure between the upper glass panels to prevent condensation inside the hood. These wires are simultaneously under high voltage, which generates an electric field that attracts ions. A heated trough surrounding the entire top of the glass hood is powered by electricity. A curved tube supplies isopropyl alcohol, which flows into the trough. The alcohol moves from the warmer upper part of the chamber to the cooler lower part, where it evaporates and dissipates, then condenses into tiny droplets and returns to the tank. Just above the thin layer of liquid covering the bottom, a region of supersaturated alcohol vapour forms. This region is the only place where charged particles from internal or external sources create ions as they pass through it. Tiny droplets of alcohol cling to these ions, creating a visible cloud track. The length and location of this track gives information about the composition of the ionising particles.

The designed chamber was placed on a square table with a length of 90 to 100 cm and a height of 30 to 60 cm. Throughout the experiment, the cloud chamber was fully shielded from direct overhead light and the vents were not obstructed. For best observing conditions, the entire experiment took place in the dark.

Protons, mesons, electrons, and alpha particles — all of which have an electrical charge— record the tracks left by this diffusion chamber. You may determine which particle passed through the cloud chamber, how fast it traveled (energy), and whether it collided or deflected during flight by observing the differences in the particle's trails. The alcohol vapor that is diffusing to the black plate from top to bottom liquefies (condenses into droplets) as soon as it gets close to the cooled plate.

There is a layer of liquid alcohol vapour, about 1-2 mm thick, above which the vapour has not completely liquefied. Drop formation, and hence cloud formation, can be intentionally induced in this layer by, for example, small dust particles (condensation nuclei) or passing radiation particles. Radiation particles "damage" (ionize) many alcohol molecules during flight; these molecules can then take on considerably larger alcohol droplets and appear visible to us. On Figure 4, they form the cloud track.

Figure 4 – Cloud chamber: the formation of cloud tracks

The first white tracks on the black surface appeared five minutes after the start of work. To maintain high accuracy and sensitivity, the temperature inside the chute was increased.
The readings of the programmable timer were set to the automatic mode of operation of the cloud camera. In addition, the base of the camera was equipped with a hole in which artificial radiation sources are supposed to be inserted.

3. Results and Discussion

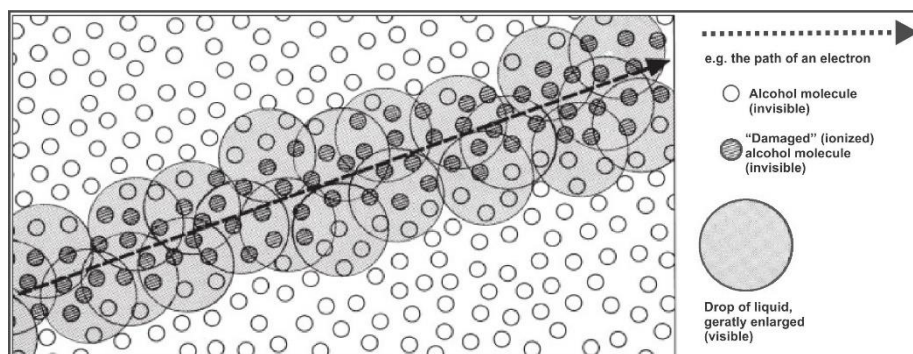Unless they are separated in a carefully insulated environment, the radioactive particles described in the previous section will always be present as background radiation. When radioactive events like decay are being studied, it is necessary to subtract the background radiation, which is usually measured at about 18 rpm, from the observed effects. Removing this amount is necessary for a precise analysis. Traditionally, this background radiation is measured using a tube counter connected to a counting device. But upon first examination of the cloud chamber's active region, a seemingly profusion of particle tracks would indicate that radioactive material—rather than just background radiation—is present in the chamber. A modest method is used to help identify background radiation as the true source of the particle track density.

Using a piece of type paper, hole in the middle of it that is about 0.8 cm in diameter to replicate the operation of a tube counter have been made. Lay the paper out flat on the cloud chamber's glass plate. Using one eye, look through the hole to the active part of the cloud chamber at a distance of about 10 cm from the paper. Count the twenty different "parts" of particle tracks that are visible through the hole and record the elapsed time at the same time.

This method simulates a tube counter's aperture. Particle tracks are only visible where they intersect this imagined opening. Out of all the particle trails in the cloud chamber, only those passing through a tube counter-like aperture are visible. This technique can verify the theoretical zero rate of particle detection. Observable are remnants of "clouds" made up of protons, electrons/positrons, mesons, and particles within the chamber. Short tracks and longer, narrower tracks are often visible. For now, we will concentrate on the longer but more noticeable tracks (Figure 6).
The tracks are statistically dispersed over the observation region, making it impossible to forecast the exact time and place of future track sightings. α – particles in air conditions usually have a diameter of around 5 cm, but in alcohol vapor, their range is significantly reduced. Moreover, α – particles can be absorbed by a single sheet of paper.

On the one hand, the decay of a radioactive nucleus might release α – particles inside the chamber. On the other hand, it is possible that protons—which have a lot of energy—are produced in the atmosphere during secondary radiation processes. These powerful protons are able to pass past the glass shielding and inside the chamber. Then, when they enter the chamber, if their energy is low enough to interact with the atomic electrons of the gas inside, they leave behind α – particles like tracks (Figure 7).

Figure 6 – Track produced by an α – particle
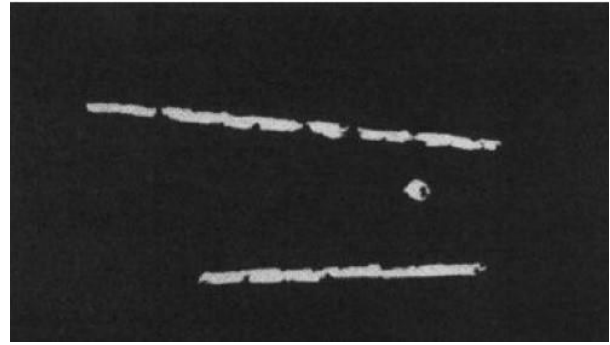
Figure 7 – Track produced by protons

The supersaturated alcohol vapor layer only permits the identification of a single location as an ionization trail when it is penetrated vertically. When the observer directs attention towards the thin and, to some extent, significantly elongated tracks (tracks exhibiting low drop density), a notable abundance of track manifestations may cause perplexity. Therefore, it is recommended to meticulously consider specific characteristics—namely, the length of these tracks.

Primarily, observers should endeavor to identify a thin, linear, and prolonged trajectory extending across the entire observation area. This trajectory is indicative of particularly swift electrons (Figure 8). Conversely, electrons moving at a slower pace (i.e., possessing a lower energy content) exhibit shorter trajectories, which are partially curved or distorted (Figure 9) due to deviation.

Figure 8 – A track produced by an electron
having a high energy content
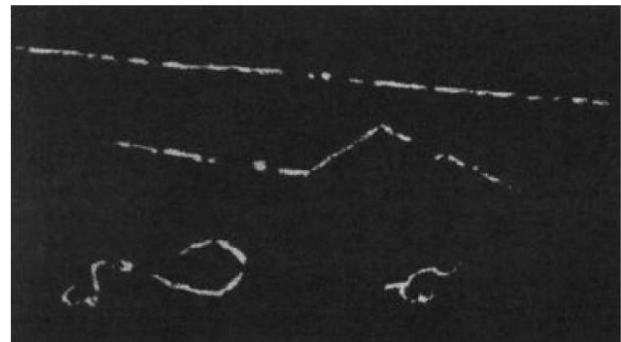
Figure 9 – Repeatedly deviating β-particles
create a track

Because of the numerous atoms' deviations in the steam layer, electrons with very low energy content produce short trajectories that appear ornate or convoluted (Figure 10).

Figure 10 – Tracks made up of β - particles with less energy

When beta β-particles with low energy pass through a diffusion chamber, they ionize the supersaturated alcohol vapor above the thin liquid layer at the bottom, resulting in short, ornate, or convoluted tracks. These tracks are distinctive due to the numerous deviations and interactions the low-energy β-particles experience with atoms in the vapor layer. The short length of these tracks indicates the lower energy of the particles, while the convoluted appearance reflects the frequent scattering events they undergo. These visible trails, formed within the carefully controlled environment of the chamber, provide valuable information about the energy and behavior of β-particles. The intricate nature of the tracks aids in distinguishing low-energy β-particles from other types of ionizing particles, offering insights into their interactions and properties.

In the Cloud chamber, mesons—which make about 90% of secondary cosmic rays—can also be found. Because m-mesons have an elementary charge that can be either positive or negative and because their weight is equivalent to 207 times that of an electron, they play a significant role in this process. High energy mesons produce trajectories that resemble the tracks left by electrons. On the other hand, heavily regulated mesons ionize and create tracks that are almost exactly like those of - particles. As a result, it will be exceedingly challenging to determine if one is looking at protons, electrons, mesons, or particles in a given instance (Figure 11).
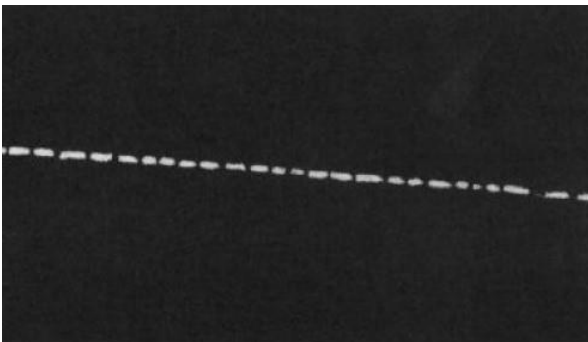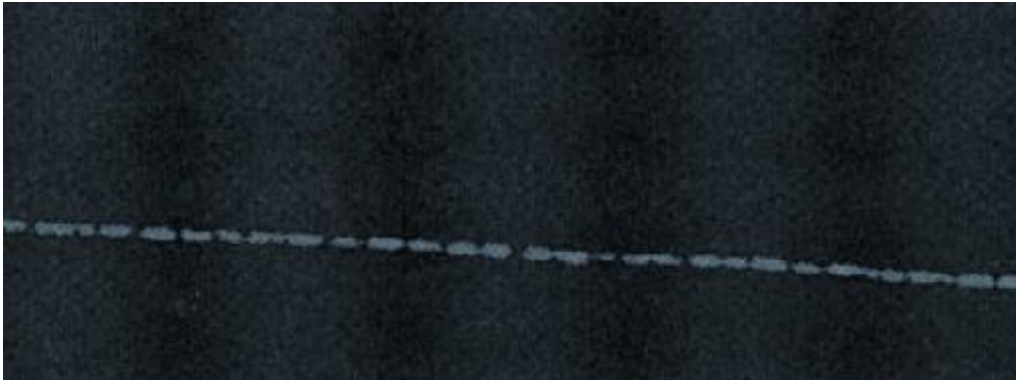

Figure 11 – Track produced by a meson

When a meson passes through a diffusion chamber, it ionizes the supersaturated alcohol vapor just above the thin liquid layer at the bottom, creating a visible cloud track. This track, characterized by its intermediate length and narrower width compared to heavier particles like alpha particles, allows for detailed analysis. The track's curvature provides insight into the meson's momentum and energy, while any bends or kinks can indicate collisions or deflections. Additionally, the meson's inherent instability might be observed through sudden changes in the track, marking decay events. These visible trails, formed within the controlled environment of the chamber—shielded from direct light and regulated for temperature and voltage—offer valuable data for identifying the meson and understanding its interactions and properties.

4. Conclusions

In conclusion, it should be noted that the development and improvement of diffusion chambers have become important milestones in research in the field of particle physics. Thanks to careful experiments, it was possible not only to optimize the camera parameters to improve particle detection, but also to conduct a thorough assessment of background radiation levels. This definition is important to minimize interference and ensure the accuracy of particle observations. Moreover, recent advances have made it possible to visualize α – particles and masons inside these chambers, shedding light on their behavior and interactions in ways previously unattainable. These achievements highlight the crucial role of diffusion chambers as indispensable tools in uncovering the mysteries of the subatomic world and deepening our understanding of fundamental particles and their properties.

References

[1]   R. A. Millikan, "History of research in cosmic rays," *Nature*, vol. 126, no. 3166, 1930, doi: 10.1038/126014A0.

[2]   R. A. Millikan, "Remarks on the history of cosmic radiation," *Science (80-.).*, vol. 21, no. 1851, pp. 640–641, Jun. 1930, doi: 10.1126/SCIENCE.71.1851.640/ASSET/CA7999E5-1117-40F6-AAC9-C8FCDEA52D81/ASSETS/SCIENCE.71.1851.640.FP.PNG.

[3]   K. G. McCracken, "Variations in the Cosmic-Ray Rigidity Spectrum," *Phys. Rev.*, vol. 113, no. 1, p. 343, Jan. 1959, doi: 10.1103/PhysRev.113.343.

[4]   F. B. McDonald, "Primary Cosmic-Ray Intensity near Solar Maximum," *Phys. Rev.*, vol. 116, no. 2, p. 462, Oct. 1959, doi: 10.1103/PhysRev.116.462.

[5]   A. Bertelsmann and R. H. Heist, "Nucleation of 1-Pentanol Using a Thermal Diffusion Cloud Chamber," *Aerosol Sci. Technol.*, vol. 28, no. 3, pp. 259–268, Jan. 1998, doi: 10.1080/02786829808965526.

[6]   N. Schaeffer, F. Utheza, F. Garnier, and G. Lauriat, "Stable stratification alteration in a thermal diffusion cloud chamber," *J. Chem. Phys.*, vol. 113, no. 18, pp. 8085–8092, Nov. 2000, doi: 10.1063/1.1315358.

[7]   F. A. Abd El-Salam and L. Sehnal, "The effects of the terrestrial infrared radiation pressure on the earth's artificial satellite dynamics," *Appl. Math. Comput.*, vol. 162, no. 3, pp. 1431–1451, Mar. 2005, doi: 10.1016/J.AMC.2004.03.019.

[8]   D. Jones, "Terrestrial myriametric radiation from the earth's plasmapause," *Planet. Space Sci.*, vol. 30, no. 4, pp. 399–410, Apr. 1982, doi: 10.1016/0032-0633(82)90046-0.

[9]   R. H. Heist, A. Kacker, and J. Brito, "NUCLEATION AND GROWTH IN THE DIFFUSION CLOUD CHAMBER II STEADY STATE NUCLEATION," *Chem. Eng. Commun.*, vol. 28, no. 1–3, pp. 117–125, Jun. 1984, doi: 10.1080/00986448408940126.

[10]   F. T. Ferguson, R. H. Heist, and J. A. Nuth, "Vapor transport within the thermal diffusion cloud chamber," *J. Chem. Phys.*, vol. 113, no. 17, pp. 7398–7405, Nov. 2000, doi: 10.1063/1.1312381.

[11]   R. H. Heist, A. Bertelsmann, D. Martinez, and Y. F. Chan, "Thermal diffusion cloud chamber: new criteria for proper operation," *Atmos. Res.*, vol. 65, no. 3–4, pp. 189–209, Jan. 2003, doi: 10.1016/S0169-8095(02)00149-7.

[12]   J. Smolík and J. Vašáková, "Experimental Study of Thermodiffusiophoresis By Use of a Thermal Diffusion Cloud Chamber," *Aerosol Sci. Technol.*, vol. 14, no. 4, pp. 406–417, Jan. 1991, doi: 10.1080/02786829108959502.

Information about authors:

Dastan Zhumanov – Master Student, Satbayev University, Institute of Automation and Information Technologies, 22a Satpaev Str., Almaty, Kazakhstan, dastan.zhumanov.02@mail.ru

Cholpon Maripova – Master Student, Kyrgyz State Technical University, Department of Physics, 66, Ch.Aitmatov Ave., Bishkek, Kyrgyzstan, cholpon.maripova@mail.ru

Author Contributions:

Dastan Zhumanov – concept, methodology, resources, data collection, testing, modeling.
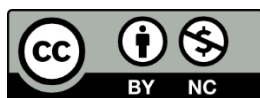*Cholpon Maripova* – analysis, visualization, interpretation, drafting, editing, funding acquisition.

Conflict of Interest. The authors declare no conflict of interest.

Use of Artificial Intelligence (AI): The authors declare that AI was not used.

Determining magnetic field strength as a function of current in Helmholtz coils

Nazerke Erzhanova*

Astana International University, School of Natural Sciences, 8 Kabanbay ave., Astana, Kazakhstan
*Correspondence: nazerke.erzhanova@internet.ru

Abstract. This study investigates the correlation between the magnetic field strength generated by two Helmholtz coils and the current passing through them. Utilizing a 100 Ohm, 1.8 A rheostat, the Helmholtz coils are connected to a variable power source (0-20V, 0-5A), ensuring stable positioning. The magnetic field at the center of the coils is precisely measured using a digital Teslameter with a Hall probe, as the current is incrementally adjusted. A digital multimeter, equipped with multiple operational modes, facilitates data collection and ensures accuracy. The empirical validation of theoretical predictions is achieved by plotting magnetic field strength against current. Adherence to stringent safety protocols, such as temperature monitoring and secure electrical connections, is maintained throughout the experiment. Helmholtz coils are mounted on a robust core assembly using supports, clamps, and rods to ensure alignment and stability. The experimental setup includes the calculation of the calibration factor and the horizontal flux density as a function of coil current. Additionally, the maximum needle deflection at 4 A allows for the measurement of the angle between the coil axis and the "north/south" direction.
Keywords: Helmholtz coils, magnetic field strength, current variation, digital teslameter, calibration factor.

1. Introduction

The magnetic field of Earth is an important component of the geophysical environment of the planet and has been studied by scientists for many years. This magnetic field, which is derived from the dynamo action in the fluid outer core of the Earth, has a significant impact on a number of natural and manmade processes. Geodynamics, tectonics, and the Earth's evolutionary history are all greatly aided by an understanding of the origin, structure, and dynamic changes of the geomagnetic field. By using satellite missions and ground-based observatories, exact measurements and analysis are used to reach this full understanding [1], [2], [3].

The geodynamo, or motion of molten iron and nickel in the outer core, is the primary source of the Earth's magnetic field [4]. Convection currents generated by the heat created by the radioactive decay of materials within the Earth are what propel this dynamo action [5]. With magnetic poles close to the geographic poles, the resulting magnetic field is mostly dipolar. However, because of the dynamic nature of the geodynamo process, the field also displays intricate non-dipolar components that change over time [6], [7].

Long-term, continuous records of the Earth's magnetic field have been made possible thanks in large part to ground-based magnetic observatories. These observatories use fluxgate magnetometers and proton precession magnetometers to measure the three components of the geomagnetic field: intensity, inclination, and declination. These data are essential for tracking secular variations, spotting magnetic abnormalities, and researching unusual events such abrupt shifts in the secular variation's rate, or geomagnetic jerks [8], [9].

Utilizing cutting-edge technologies and approaches, recent studies of the Earth's magnetic field have improved our comprehension of this intricate geophysical phenomenon. Improved modeling methods, high-resolution observations, and the local and global effects of magnetic field fluctuations have been the main topics of these investigations [10], [11].

The use of high-resolution satellite missions has been one of the most important developments in the study of the Earth's magnetic field. Launched in 2013, the European Space Agency's Swarm mission consists of three identical satellites operating in a constellation to monitor magnetic signals with previously unheard-of accuracy from the Earth's core, mantle, crust, oceans, ionosphere, and magnetosphere [12], [13]. Swarm data have given deep insights into core-mantle interactions, the dynamics of the geodynamo, and the impact of external sources like solar activity on the geomagnetic field. Researchers may now examine the fine-scale characteristics of the Earth's magnetic field and develop more precise global geomagnetic models thanks to the Swarm mission. For instance, complex structures of magnetic anomalies and secular fluctuation have been discovered by recent analysis of Swarm data, which has improved our comprehension of the underlying geodynamic processes. Furthermore, studying geomagnetic jerks—rapid variations in the geomagnetic field—and their consequences for the mechanics of the Earth's core have been made possible thanks in large part to Swarm data [13].

With the availability of high-resolution data, research on abrupt variations in the Earth's magnetic field, or geomagnetic jerks, has advanced dramatically. Studying geomagnetic jerks, which are abrupt increases in the rate of secular fluctuation, can provide important details about the inner workings of the Earth. The goal of recent studies has been to determine the cause of these jerks and how core-mantle interactions relate to them. For instance, a study that discovered a geomagnetic jerk that happened in 2015 using Swarm data shed light on the underlying mechanics. The results imply that these quick changes could be related to modifications in the flow patterns caused by compositional and thermal convection processes in the Earth's outer core [14], [15].

Thanks to recent developments, the useful applications of geomagnetic field investigations are growing. Improved geomagnetic models improve GPS and compass accuracy, which is important for aerial and marine navigation. Extensive magnetic surveys are used in mineral exploration to find subsurface mineral deposits, which benefits the mining sector [16].

In this paper, to better understand the properties of magnetic fields, two kinds of Helmholtz coils, round and square, of equal size, have been used.

2. Methods

This experiment looks at the relationship between the current flowing through two Helmholtz coils and the strength of the magnetic field they produce. To control current flow, the Helmholtz coils are firmly installed and linked to a variable power source with 0-20V and 0-5 A via a rheostat of 100 Ohm and 1.8 A. As the current is gradually changed, the magnetic field at the coils' center is precisely measured using a digital Teslameter fitted with a Hall probe. A digital multimeter in operating mode of 600V AC/DC, 10A AC/DC, 20 MΩ, 200 μF, 20 kHz, $-20°C - 760°C$ makes data collecting easier and ensures dependability by taking several readings.

By constructing a graph that plots magnetic field strength versus current using the obtained data, theoretical predictions are empirically validated. Strict safety precautions are followed during the experiment, such as keeping an eye on the temperatures of the equipment and making sure the electrical connections are secure to guarantee precise and safe measurements.

Using the proper stands, clamps, and rods with 250 mm of length and diameter of 10 mm , the Helmholtz coils are firmly fixed to a sturdy core assembly to guarantee alignment and stability during the experiment.

The rheostat and the multimeter that is used as an ammeter are used to connect the Helmholtz coils, along with the installed space holders, to the DC generator in series (a linkage of equally-

numbered connections). The barrel base of the Hall probe should point inward toward the coil axis in the middle of the Helmholtz arrangement when it is placed on the support rod (Figure 1).
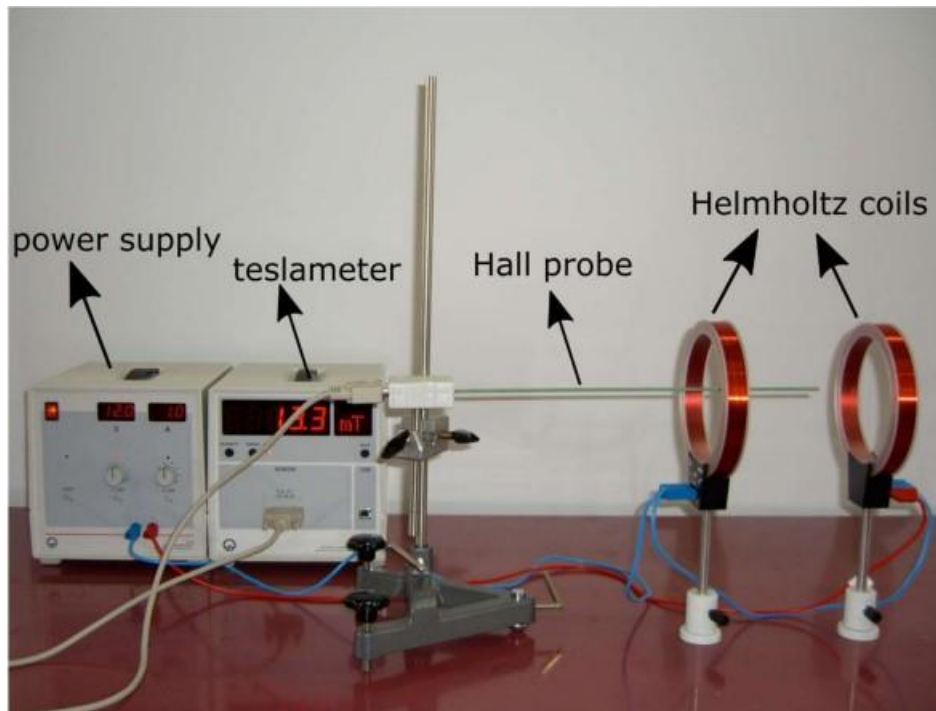
Figure 1 – Experimental equipment

The magnetometer's graded circle was then turned into the vertical plane while the coils were devoid of electricity, enabling the magnetic needle to display the inclination angle υ_1. The spin axis was carefully positioned to match the "north/south" direction accurately. The magnetometer was turned 180 degrees and reinstalled in the vertical plane to confirm υ_2.

The Teslameter's zero-point position was carefully calibrated prior to the measurements starting. The magnetometer, which had a leveled graduated circle, was being positioned between the coils using a barrel base, stand tube, and visual judgment to have the center of the graduated circle roughly aligned with the center of each pair of coils. Originally, when there was no current running through the coils, the direction "north/south" was marked on the graded circle. The magnetic needle was being gently deflected from its resting position many times to verify precise orientation, and the instrument was being carefully tapped to reduce friction resistance.

By measuring the deflection angle of the magnetic needle from its resting position in response to tiny currents given to the coils, the horizontal component of the Earth's magnetic field was found. The measurement series needed to be rerun if the coil current's polarity was switched. Readings from both ends of the needle were being considered in order to determine the exact angle.

3. Results and Discussion

In this paper, for a better understanding of the properties of magnetic fields, they were generated by two kinds of Helmholtz coils, round and square of equal size. The geometric sizes of the two coil pairs are set to the same value: the side length of the square coil pair is 100 mm, and the radius of the circular coil pair is 50 mm, in order to analyze the magnetic fields of the two coil pairs.

According to the data, the magnetic field distribution on the Y-axis of the square and circular coils is displayed in Figure 3. From this, a sizable area of uniform magnetic field in both coils can be obtained. The horizontal flux density ^hB_H of the two coils in this setup must be calculated as a function of the coil current I_H. The accompanying graphic representation aids in the determination of the

calibration factor $K = \dfrac{^h B_H}{I_H}$ (Figure 2). By short-circuiting the resistor, removing the ammeter, and setting the coil current to about 4 A, the maximum needle deflection was achieved. This allowed for the determination of the angle α (Figure 3) between the "north/south" direction and the axis of the two coils.
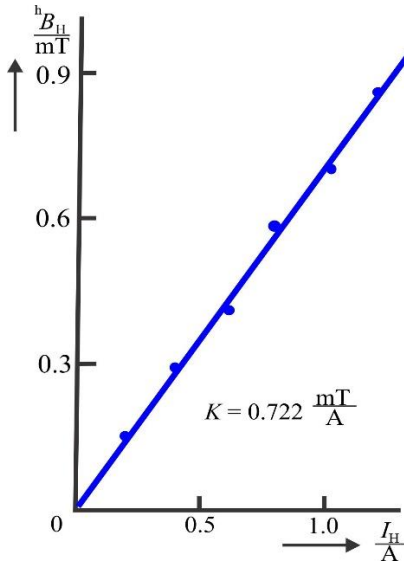
Figure 2 – Function of calibration for the two Helmholtz coils
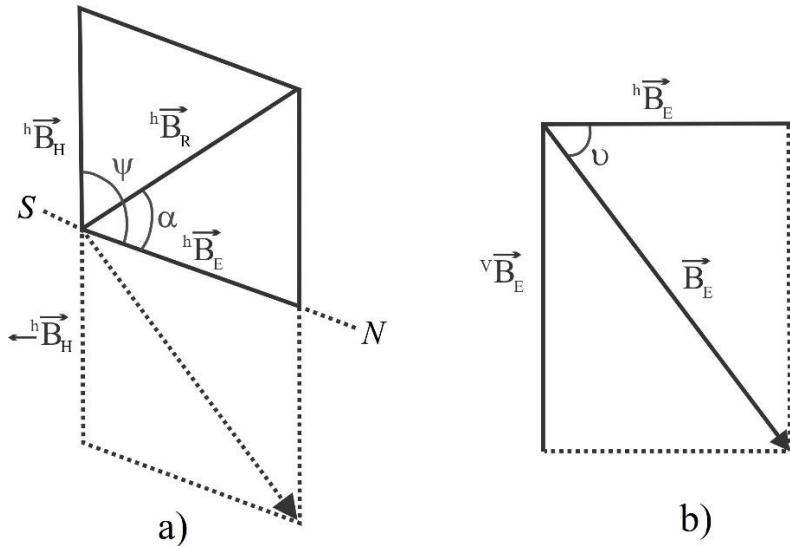
Figure 3 – The magnetic flux densities are shown as a vector graphic with: a) horizontal plane and b) vertical plane

It is possible to look at the connection between the measured values and the theoretical predictions. On Figure 4 the horizontal component of the Earth's magnetic field can be directly measured by the slope of this function, when $I_H * K$ is seen as a function of $\dfrac{sin\alpha}{sin\beta}$.
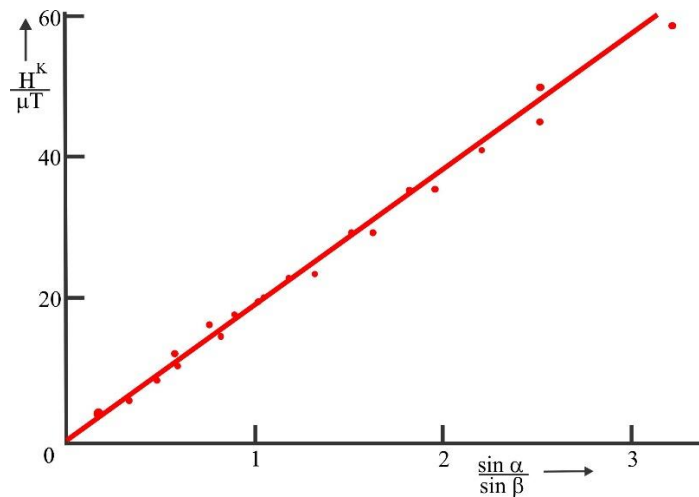
Figure 4 – Linear function of the Earth magnetic field's horizontal component of the magnetic flux density

This correlation shows that this component was successfully measured and captured by the experiment. Moreover, the measured angle of inclination and the vertical component of the Earth's magnetic field were inferred from the data shown ($^h B_H$ = 18.8 mkT) according Figure 2b. The accuracy of our experimental setup and measurement procedures in defining both components of the

Earth's magnetic field is validated by the consistency between the experimental results and theoretical expectations:

$$\upsilon = \tfrac{1}{2}(\upsilon_1 + \upsilon_2) = \tfrac{1}{2}(67^o + 68^o) = 67.5^o \tag{1}$$

$$B_E = B_E \tan \upsilon = 46.3 \; \mu T \tag{2}$$

Combining the horizontal component B_h and vertical component B_v found in the experiment yields the total magnetic flux density. These components must be added vector-wise in the calculation, usually using the following equation:

$$|B_E| = \sqrt{(B_E vertical)^2 + (B_E horizontal)^2} = 50.2 \; mkT \tag{3}$$

This calculation provides a comprehensive measure of the total magnetic flux density at the location of the experiment, considering both the horizontal orientation relative to the Earth's surface and the vertical orientation towards or away from the Earth. The accuracy of this calculation is essential for understanding the overall strength and orientation of the Earth's magnetic field in the vicinity of the experiment.

For applications that require constant magnetic fields, it is critical to optimize design and ensure field uniformity by comparing the magnetic field data of square and circular Helmholtz coils. Evaluating the errors associated with each coil shape provides insights into their precision and reliability, aiding in the selection of the appropriate configuration for specific needs in industrial processes. This comparative analysis also offers theoretical and practical insights into how different geometries affect magnetic fields, guiding future coil designs and contributing to the development of new technologies. Additionally, understanding the trade-offs between performance, manufacturing complexity, and cost can lead to more informed decisions in coil design and application.

The Table 1 presents the calculated magnetic field data for two different types of Helmholtz coils: circular and square. Measurements were taken at various distances from the center of the coil, with corresponding calculated magnetic field strengths and associated errors (in percentages).

Table 1 – Obtained data of different type of Helmholtz coils

Circular Helmholtz coils			Square Helmholtz coils	
y, mm	Calculated data, uT	Error, %	Calculated data, uT	Error, %
0	35.98	0.752	32.52	0.992
5	35.95	0.751	32.53	0.991
10	35.92	0.761	32.57	1.001
15	35.68	0.776	32.41	1.005
20	35.11	0.891	32.12	1.012

For the circular Helmholtz coils, the calculated magnetic field strength at the center (y = 0 mm) is 35.98 µT with an error of 0.752%. As the distance increases, the calculated magnetic field slightly decreases, reaching 35.11 µT at y = 20 mm, with the error increasing to 0.891%.

For the square Helmholtz coils, the initial calculated magnetic field strength at the center is 32.52 µT with an error of 0.992%. Similar to the circular coils, the magnetic field strength decreases with distance, recording 32.12 µT at y = 20 mm, and the error increases to 1.012%.

These data demonstrate the variation in magnetic field strength and associated errors between the circular and square Helmholtz coils across different distances from the center.

4. Conclusions

In summary, this experiment effectively used accurate measuring techniques with a digital Teslameter and magnetometer to examine the properties of the magnetic field generated by two Helmholtz coils and the components of the Earth's magnetic field. We found connections that confirmed theoretical assumptions by measuring the magnetic field intensities $^h B_H = 18.8 \; mkT$ by

vertical component that resulted from methodically adjusting the current through the coils. The geographical distribution and intensity of the magnetic field in our experimental setup were better understood by calculating the overall magnetic flux density and determining the horizontal and vertical components of the Earth's magnetic field, that was indicated $B_E = 50.2$ *mkT*. These discoveries are important for applications in geophysics, navigation, and related domains and further our understanding of magnetic field interactions. To better understand Earth's magnetic field dynamics, future research might concentrate on improving measuring methods and investigating differences in magnetic field intensity across different geographical locations.

The comparative analysis of circular and square Helmholtz coils reveals notable differences in their magnetic field strengths and associated errors across various distances. For instance, at the center (y = 0 mm), the circular Helmholtz coils generate a magnetic field strength of 35.98 µT with an error of 0.752%, while the square Helmholtz coils produce 32.52 µT with an error of 0.992%. As the distance increases to 20 mm, the magnetic field strength for circular coils decreases to 35.11 µT with an error of 0.891%, and for square coils, it decreases to 32.12 µT with an error of 1.012%. These findings are essential for optimizing coil design to achieve uniform magnetic fields, ensuring high precision, and balancing cost and manufacturing complexity. By understanding these differences, more informed decisions can be made in selecting the appropriate coil geometry, enhancing the effectiveness and efficiency of applications in scientific research, medical imaging, and industrial processes.

References

[1] F. Donadini, M. Korte, and C. Constable, "Millennial variations of the geomagnetic field: From data recovery to field reconstruction," *Space Sci. Rev.*, vol. 155, no. 1–4, pp. 219–246, Aug. 2010, doi: 10.1007/S11214-010-9662-Y/METRICS.

[2] M. Dumberry and C. C. Finlay, "Eastward and westward drift of the Earth's magnetic field for the last three millennia," *Earth Planet. Sci. Lett.*, vol. 254, no. 1–2, pp. 146–157, Feb. 2007, doi: 10.1016/J.EPSL.2006.11.026.

[3] M. Korte, C. Constable, F. Donadini, and R. Holme, "Reconstructing the Holocene geomagnetic field," *Earth Planet. Sci. Lett.*, vol. 312, no. 3–4, pp. 497–505, Dec. 2011, doi: 10.1016/J.EPSL.2011.10.031.

[4] E. M. King and B. A. Buffett, "Flow speeds and length scales in geodynamo models: The role of viscosity," *Earth Planet. Sci. Lett.*, vol. 371–372, pp. 156–162, Jun. 2013, doi: 10.1016/J.EPSL.2013.04.001.

[5] M. Kono and P. H. Roberts, "Definition of the Rayleigh number for geodynamo simulation," *Phys. Earth Planet. Inter.*, vol. 128, no. 1–4, pp. 13–24, Dec. 2001, doi: 10.1016/S0031-9201(01)00274-6.

[6] M. Schrinner, D. Schmitt, R. Cameron, and P. Hoyng, "Saturation and time dependence of geodynamo models," *Geophys. J. Int.*, vol. 182, no. 2, pp. 675–681, Aug. 2010, doi: 10.1111/J.1365-246X.2010.04650.X/2/M_182-2-675-EQ016.JPEG.

[7] M. D. Menu, L. Petitdemange, and S. Galtier, "Magnetic effects on fields morphologies and reversals in geodynamo simulations," *Phys. Earth Planet. Inter.*, vol. 307, Oct. 2020, doi: 10.1016/j.pepi.2020.106542.

[8] N. Olsen *et al.*, "The Swarm satellite constellation application and research facility (SCARF) and Swarm data products," *Earth, Planets Sp.*, vol. 65, no. 11, pp. 1189–1200, Nov. 2013, doi: 10.5047/EPS.2013.07.001/TABLES/4.

[9] C. C. Finlay, N. Olsen, and L. Tøffner-Clausen, "DTU candidate field models for IGRF-12 and the CHAOS-5 geomagnetic field model International Geomagnetic Reference Field - The Twelfth generation," *Earth, Planets Sp.*, vol. 67, no. 1, pp. 1–17, Dec. 2015, doi: 10.1186/S40623-015-0274-3/FIGURES/11.

[10] J. Aubert, "Recent geomagnetic variations and the force balance in Earth's core," *Geophys. J. Int.*, vol. 221, no. 1, pp. 378–393, Apr. 2020, doi: 10.1093/GJI/GGAA007.

[11] C. J. Davies, R. K. Bono, D. G. Meduri, J. Aubert, S. Greenwood, and A. J. Biggin, "Dynamo constraints on the long-term evolution of Earth's magnetic field strength," *Geophys. J. Int.*, vol. 228, no. 1, pp. 316–336, Sep. 2021, doi: 10.1093/GJI/GGAB342.

[12] G. Hulot *et al.*, "Swarm's absolute magnetometer experimental vector mode, an innovative capability for space magnetometry," *Geophys. Res. Lett.*, vol. 42, no. 5, pp. 1352–1359, Mar. 2015, doi: 10.1002/2014GL062700.

[13] R. Tozzi, M. Pezzopane, P. De Michelis, and M. Piersanti, "Applying a curl-B technique to Swarm vector data to estimate nighttime F region current intensities," *Geophys. Res. Lett.*, vol. 42, no. 15, pp. 6162–6169, Aug. 2015, doi: 10.1002/2015GL064841.

[14] S. Maus, "Mysterious misalignments between geomagnetic and stellar reference frames seen in CHAMP and Swarm satellite measurements," *Geophys. J. Int.*, vol. 203, no. 3, pp. 1873–1876, Dec. 2015, doi: 10.1093/GJI/GGV409.

[15] Q. Li *et al.*, "Performance Analysis of GPS/BDS Broadcast Ionospheric Models in Standard Point Positioning during 2021 Strong Geomagnetic Storms," *Remote Sens. 2022, Vol. 14, Page 4424*, vol. 14, no. 17, p. 4424, Sep. 2022, doi: 10.3390/RS14174424.

[16] X. Li, H. Cai, D. Li, C. Geng, L. Chen, and J. Xu, "Analysis of the influence of geomagnetic storms on the ionospheric model of beidou/GPS system," *Lect. Notes Electr. Eng.*, vol. 388, pp. 503–510, 2016, doi: 10.1007/978-981-10-0934-1_43/FIGURES/4.

Information about authors:
Nazerke Erzhanova – Master Student, School of Natural Science, Astana International University, 8 Kabanbay ave., Astana, Kazakhstan, nazerke.erzhanova@internet.ru

Author Contributions:
Nazerke Erzhanova – concept, methodology, resources, data collection, testing, modeling, analysis, visualization, interpretation, drafting, editing, funding acquisition.
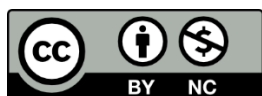
Conflict of Interest: The authors declare no conflict of interest.

Use of Artificial Intelligence (AI): The authors declare that AI was not used.

Efficient Light Coupling and Propagation in Fiber Optic Systems

Vladimir Myasnikov*

Phystech School of Aerospace Technology, Moscow Institute of Physics and Technology, 9 Institutskiy per., Dolgoprudny, Russian Federation
*Correspondence: myasnokov_vld@mail.ru

Abstract. This study explores the propagation of light in optical fibers, focusing on the fundamental principles and practical implications for fiber optic technologies. By analyzing the wave equation, the research demonstrates that light propagates as cylindrical waves within the fiber, contrasting with spherical waves in free space. The study highlights the significance of Gaussian beams, particularly from helium-neon lasers, finding a beam waist radius of approximately 12.6 micrometers and its position about 1.25 micrometers from the focus. These parameters are critical for optimizing laser beam coupling into the fiber. The research also measures the light transit time through a 100-meter fiber, revealing a light speed of approximately 2×10^8 m/sec, which is influenced by the fiber's refractive index. Additionally, the relationship between diode laser output power and injection current was investigated, demonstrating a linear correlation crucial for practical applications. The findings emphasize the importance of accurate measurements and configuration in improving fiber optic communication and laser performance. This comprehensive analysis provides valuable insights into the design and optimization of optical fiber systems, contributing to advancements in communication and laser technologies.
Keywords: fiber optics, Gaussian beams, light propagation, laser coupling, numerical aperture.

1. Introduction

The term "fiber optics" describes the technique and media used to transmit data as light pulses down a thread of glass or plastic Figure 1 [1]. Applications for it are found in: communications: sends out infrared light pulses to carry information, including cable television signals, internet signals, and phone calls [2]. Sensors: transmits data from a distant sensor to the electronics for signal processing [3]. Medical: fiber optic cable known as endoscopy, they utilized as light guides in imaging and illumination components for minimally invasive surgical techniques [4].
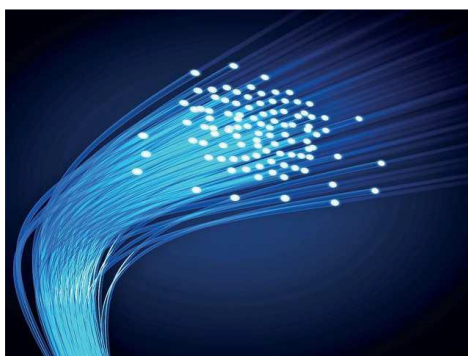

Figure 1 – Cables with fiber optics [1]

The definition of total reflection is the reflection of light at incidence angles equal to or greater than the critical angle of total reflection at the transition from an optically denser medium to one that is optically less dense. A laser diode's beam is processed so that it can be linked into a monomode fiber [5]. The issues pertaining to the coupling of the beam into the fiber are assessed and confirmed. As a result, a low frequency signal travels via the fiber. The fiber's numerical aperture is noted. It is possible to measure the light's transit time through the fiber and calculate its internal velocity. Ultimately, the measurement of the diode laser's relative output power as a function of supply current yields the device's properties, including "slope efficiency" and "threshold energy."

Recognizing the fundamentals of fiber optics application [6].
1. Couple the laser beam into the fiber and modify the configuration so that the fiber's exit produces the highest possible output power.
2. Show how an LF signal can be sent across a fiber.
3. Calculate the fiber's numerical aperture.
4. Calculate the light's velocity within the fiber by measuring the light's transit time through it.
5. Ascertain the diode laser's relative output power in relation to the supply current.

The standard guidelines for safe experimenting in science classes apply to this particular project. Being able to use information more quickly than others is a fundamental human ambition. The concept of employing light signals to communicate data by passing them through a medium that conducts light was put out by the paper [7]. However, Buchholz's concept was not implemented until 1962 with the invention of the semiconductor laser, which used fibers as a light transmission medium in conjunction with these types of lasers. All of a sudden, light could be generated and modulated with ease using powerful light sources. Using laser diodes and fibers to transmit signals has become an essential technological advancement in modern times. Probably one of the most significant developments of this century has been the ongoing advancement of this field. It is worth noting that after the development of communication technology, navigation fiber laser deserves special attention [8]. As this new technology is based on established ideas, it does not require any new insights. Nevertheless, there is a technical implementation as light needs to be guided inside a 5 μm diameter fibre.

The physical processes that are fundamental to fibre optics were previously demonstrated by the experiment of resonant light scattering at total internal reflection at solid/liquid interfaces [8]. It is worth noting that the experiment presented in Figure 2 reveals some states at its d >>λ; for a fibre with multiple modes d >λ; for a monochrome fibre d = λ.
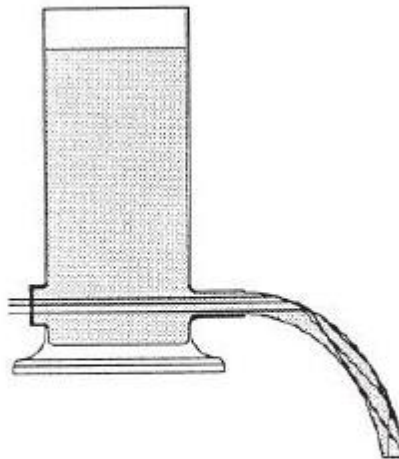

Figure 2 – Total internal reflection

This results in additional effects for the modern fibers that cannot be fully explained by total reflection. Their comprehension is particularly crucial for optical communication technologies [9].

Fiber optic systems have become the backbone of modern communication networks, offering unparalleled bandwidth and data transmission rates compared to traditional copper cables. The effectiveness of these systems is heavily reliant on the efficient coupling and propagation of light within optical fibers. Efficient light coupling refers to the process of transferring optical power from a light source into the fiber with minimal losses, while efficient propagation involves maintaining the integrity of the light signal as it travels through the fiber, minimizing attenuation and distortion.

In optical communication systems, the fundamental challenge of light coupling stems from the mismatch between the numerical aperture (NA) of the fiber and the light source, typically a laser or light-emitting diode (LED). The efficiency of this process is influenced by factors such as alignment accuracy, fiber mode field diameter, and the lens systems used to focus the light into the fiber. Advances in coupling techniques, such as using microlenses or gradient-index lenses, have significantly improved coupling efficiency by better matching the mode fields of the light source and the fiber [10].

Propagation within optical fibers is governed by the principles of modal dispersion and attenuation. Modal dispersion occurs when different light modes travel at different velocities, causing pulse broadening and signal degradation. Attenuation, on the other hand, results from scattering and absorption losses within the fiber material. Innovations in fiber design, such as the development of photonic crystal fibers and the use of low-loss materials like silica, have addressed these issues by enhancing mode confinement and reducing attenuation [11].

The integration of advanced fabrication techniques and improved materials has led to significant advancements in fiber optic technology. For instance, the use of specialized coatings and cladding materials has reduced attenuation losses, while the implementation of mode-field adapters and precise alignment mechanisms has enhanced coupling efficiency. These developments are crucial for the deployment of high-capacity optical networks, including those used in data centers, long-haul telecommunication, and high-speed internet services [12].

Thus, efficient light coupling and propagation are critical to the performance of fiber optic systems. Ongoing research and technological advancements continue to improve these aspects, driving the development of faster and more reliable optical communication networks. Continued progress in this field promises to support the ever-increasing demand for high-speed data transmission and communication.

This work will focus on the calibration of equipment designed to evaluate the coupling efficiency and optical performance of mono-mode optical fibers. The calibration will involve setting up and checking all components of the experimental setup such as light sources, detectors and spectrum analyzers to ensure accurate and reliable measurements. This is important to obtain reliable data on fiber parameters such as attenuation coefficient, dispersion and polarization characteristics, which will allow a qualitative analysis of the efficiency of signal transmission through optical fibers.

2. Methods

The experimental setup employed in this study is designed to evaluate the coupling efficiency and optical characteristics of monomode optical fibers. The system comprises multiple modules to facilitate precise alignment, beam collimation, and fiber coupling. The following sections detail the methodology used to prepare and configure the experimental apparatus.

The monomode optical fiber used in this study is first prepared by removing the insulation from both ends through a careful scratching process that presents on Figure 3.

The fiber, which has been cut and cleaved to ensure clean ends, is then positioned into a designated groove within the fiber holder. This holder is secured using a magnet to stabilize the fiber in place. Ensuring precise placement is crucial for minimizing alignment errors during subsequent measurements. The alignment of the laser diode and the optical axis is as follows.
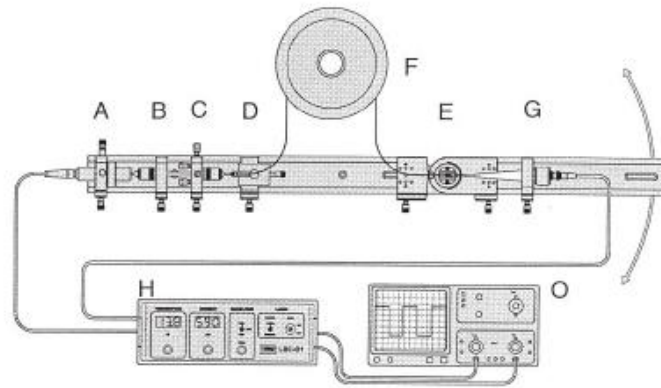
Figure 3 – Schematic diagram of the monomode fiber experimental setup

Module A contains a laser diode enclosed in a housing that features a Peltier cooler and a thermistor for temperature regulation and monitoring. The laser diode, capable of emitting a maximum power of 50 mW, is mounted on a fine-adjustment XY stage. To initiate the setup, the optical axis is aligned using an oscilloscope to visualize the modulation of the injection current. Rectangular pulses observed on the oscilloscope confirm the correct modulation.

Module B is equipped with a microscope objective that collimates the laser diode radiation. The objective is mounted on a removable plate to allow for easy interchangeability. The positioning of the collimator is adjusted such that the laser beam is rendered nearly parallel. This is achieved by fine-tuning the collimator's placement and optimizing the beam profile using the XY-displacement screws in Module A. The alignment is verified by maximizing the signal detected on the oscilloscope, ensuring that the detector does not reach saturation. To inject the diode laser beam into the fibre, the beam was first collimated using module B. If necessary, the injection current is adjusted to avoid over-driving the detector.

Module C is introduced into the setup to facilitate the coupling of the collimated laser radiation into the fiber. This module features an adjustable holder with four-axis XY movement and an objective with a shorter focal length than Module B's objective. The design of Module C aims to focus the collimated beam effectively onto the fiber, optimizing the coupling efficiency. The distance between module C and module B was fixed at 50 mm and the position of the laser beam was parallel. The beam shaping component is omitted to streamline the experimental process and simplify the initial alignment.

Module D involves the mounting of the prepared fiber onto a stage with linear displacement capabilities. This stage allows for precise adjustments in the direction of the incident beam to achieve optimal coupling between the laser and the fiber (Figure 4).
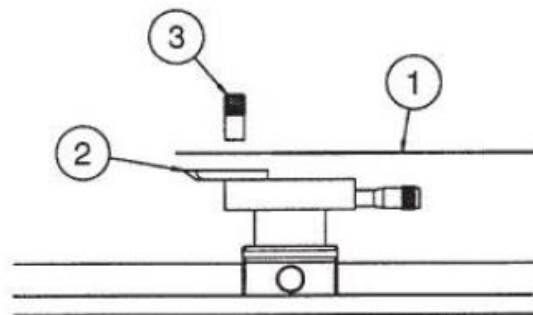

Figure 4 – Mounting module D's plug connector

The fibre adjustment holder (module D without fibre) was mounted on the rail at a distance of about 10 mm from module C. The fibre was then carefully placed on the fibre adjustment holder and inserted.

Module F contains a 100 m coil of monomode fiber, which can be used for various alignment and coupling tests. It is important to note that while multimode fibers can be employed to ease alignment due to their larger core size, this study specifically utilizes monomode fibers for its precision requirements.

Module E features a hinged angle connector with a secondary fiber holder, which lacks a linear stage but allows for the assessment of angle-dependent output power from the fiber. This module is integral for evaluating the performance of the fiber under different angular alignments.

Module G comprises a detector equipped with a PIN photodiode. The detector is connected to the preamplifier of the control unit LDC01 via a BNC cable, with the inner pin of the BNC plug in contact with the anode of the photodetector. This configuration ensures accurate detection and measurement of the optical signal transmitted through the fiber. Situated on the right guide, at a distance set by the rotary joint, the holder G with the PIN-photodiode is not too distant from the holder E. The measurement range for the fiber output power is -10 to +10 degrees. In the experiment, external interference was eliminated by the use of modulated light. The relationship between the amplitude and light intensity was proportionate.

Furthermore, an investigation was conducted into the measuring of light transit time via the fiber. The arrangement was modified to position the detector close to the fiber's end in the holder G. An oscilloscope set at 100 Hz was directly linked to the detector. The signal rising time was shortened by using a 50 Ohm resistor as a shunt. The LDC01 control unit's injection current monitor's output was linked to the second channel. Curve A is obtained by appropriately dialing the time basis on the second channel. In this instance, the installed plug connections were taken out of their holders and the fiber was left out of the installation.

The time difference T_1 at 50% rise time was measured by the prescribed curve that was shown on the first channel. When the system operates without fiber, all time delays are represented by the time T_1. Then, the fiber's power was adjusted back to its maximum.

The diode laser's relative output power was measured by finding rising supply current levels. In this instance, it is imperative to ensure that the photodiode is not saturated and to position the PIN photodiode two centimeters in front of the diode laser.

3. Results and Discussion

It is interesting to consider fibers made of glass or similar material as conductors of light. They lack magnetic dipoles, free charge carriers and electrical conductivity. Hence, the following are Maxwell's equations modified for our equation:

$$\Delta x \vec{H} = \epsilon \cdot \epsilon_0 \cdot \frac{\delta \vec{E}}{dt} \text{ and } \Delta x \vec{H} = 0 \tag{1}$$

$$\Delta x \vec{H} = \frac{\delta \vec{E}}{dt} \text{ and } \Delta x \vec{E} = 0 \tag{2}$$

Where, is the free space's dielectric constant. The unit of charge (As) divided by the unit of field strength (V/m) yields $8.859 * 10^{-12} \frac{As}{Vm}$, which is the dielectric constant of matter. It describes the extent to which an external electric field E acts on an electric dipole. The following relationship connects the susceptibility χ and the dielectric constant ϵ:

$$\epsilon = \frac{1}{\epsilon_0} \cdot (\chi + \epsilon_0) \tag{3}$$

$$\epsilon \cdot \epsilon_0 \cdot \vec{R} = \vec{D} \tag{4}$$

Is referred to as "dielectric displacement" or displacement for this reason. is the open space's total permeability. It provides the relationship between the unit of an induced voltage (V) caused by a magnetic field H and the unit of ampere-seconds. That comes to $1.256 \cdot 10^{-6} \frac{Vs}{Am}$.

Glass fibers have a circular cross section when used as wave conductors. They are made up of a refractive index core n_k. A glass cladding with a refractive index n_m marginally lower than encircles the core. Both the core's and the cladding's refractive indices are typically thought to be homogeneously distributed. It is located where the cladding and core meet. The angle θ_e at which the beam enters the fiber determines its ultimate direction. In this technique, unintentional but sometimes unavoidable radiation and cladding waves are produced. The fiber is encased in a protective covering for mechanical protection and radiation wave absorption.

Some fundamental information is shown in Figure 5 and does not require the solution of Maxwell's equations. We may say that there has to be a limiting angle for total reflection at the cladding-core boundary based on geometrical considerations:

$$\cos \theta_c = \frac{n_m}{n_k} \tag{5}$$
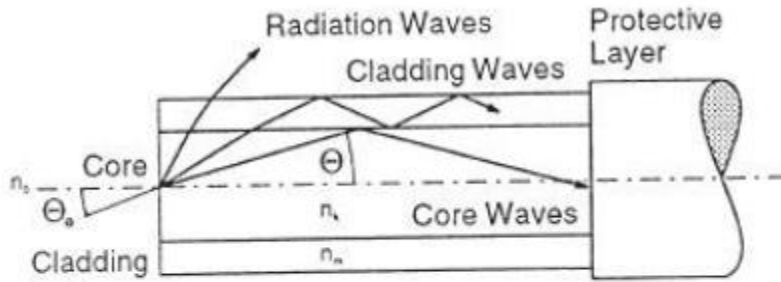
Figure 5 – Step index fibre

The equation of refraction to determine the angle of incidence of the fiber have been applied:

$$\frac{\sin \theta_{ec}}{\sin \theta_c} = \frac{n_m}{n_k} \tag{6}$$

and acquire:

$$\theta_{ec} = \arcsin\left(\frac{n_k}{n_0} \cdot \sin \theta_c\right) \tag{7}$$

Finally, using the previous equation and setting $n_0=1$ for air, it can be obtained:

$$\theta_{ec} = \arcsin\left(\sqrt{n_k^2 - n_m^2}\right) \tag{8}$$

Half of a cone's opening angle is represented by the limiting angle θ_{ec}. Every ray that enters this cone will be completely reflected into the center. Here, too, as is customary in optics, we can define a numerical aperture A:

$$A = \sin \theta_{ec} = \left(\sqrt{n_k^2 - n_m^2}\right) \tag{9}$$

The beams propagate in a screw depending on the angle at which they enter the cylindrical core through the cone. If we project the beam displacements onto the fiber's XY plane, this becomes clear. The z-axis is defined as the direction that runs along the fiber. A consistent trend is identified. In the XYplane, it can be understood as standing waves. Standing waves are referred to as oscillating modes, or just modes, in this context. These modes are also known as transverse modes since they are constructed in the XY-plane, for example, perpendicular to the z-axis. Longitudinal modes are those that are accumulated along the z-axis. This process depict in Figure 6.

Figure 6 – Spiral (A) and Meridional ray (B)

For the core, the Bessel function works well. It also required a field attenuation for the classification. A possible answer in this case is provided by the modified Hankel function $x \to 0$ and $r \to 0$ only for the range $r \leq a$ yet it goes on to infinity (cladding).
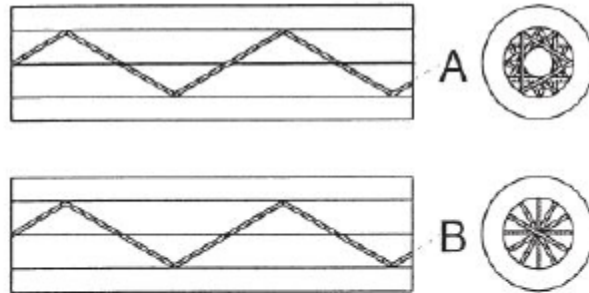
The Bessel function will be applied to the ranger $r \geq a$ (core). We will fit the Bessel and Hankel function for $r = a$ and apply the continuity conditions of the components of E and H for the transition from core to cladding to solve the difficulties at the border between the two layers.

One of the fundamental solutions is shown in Figure 7. It witnessed the formation of the electric field inside the core. It also becomes evident that the fiber's radius will determine the modes' sequence.
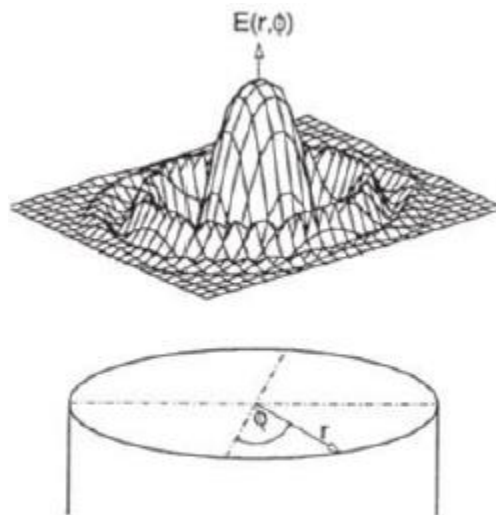
Figure 7 – Bessel function solution in the core

A major maximum at $r = 0$ and smaller maxima or minima, sometimes known as nodes, further out in the radial direction of the fibre can be seeing. The diameter of the fiber and the answer to the wave equation inside the cladding define the number of nodes.

It is necessary to confirm that the cylindrical function selected for the solution inside the cladding meets the continuity requirements for the electric and magnetic fields at the core-cladding border. In order to favor the direction of waves within the core, efforts have been undertaken to cause the radial field of the core to rapidly drop in the sheath for sheath waves. A fiber is referred to as monomode or single-mode if it is constructed so that just the primary wave is steered inside the core. It is permissible to refer to a multimode fiber in all other circumstances. One or more types of fiber are utilized, depending on the application. Let's now extract the fiber's "construction rule" from the solutions. This will enable us to ascertain the circumstances in which the fiber "accepts" an incoming wave of a specific wavelength and conducts it as a monomode fiber. An purely basic wave can only propagate if the following conditions are met:

$$0 < \frac{2\pi}{\lambda} a \sqrt{n_k^2 - n_m^2} \leq 2.405 \tag{10}$$

One crucial guideline for the fiber's design is seen in equation 10 above. If the wavelength λ and the refractive index for the cladding and core have been chosen, it fixes the radius an of the core for monomode waveguidance. The range for radius an is as follows if, for instance, the aim is to transmit the light of a helium-neon laser (wavelength 633 nm, refractive index of the shell 1.4):

$$a < 2.405 \cdot \frac{633 \cdot 10^{-9}}{2\pi\sqrt{1.5^2 - 1.4^2}} = 0.45 \ \mu m \tag{11}$$

The refractive index differential has a significant impact on the outcome. The radius a can be larger the smaller this disparity is. Nevertheless, the refractive index of the core cannot be selected to be significantly higher than the refractive index of the cladding for technological reasons. It is only possible to utilize glasses with similar temperature coefficients because the core and cladding are in close contact. The slight variation in refractive index is the result of this. For regular fibers, it is:

$$\frac{n_k - n_m}{n_k} = 2 \cdot 10^{-3} \tag{12}$$

When the core's refractive index equals 1.465. Using these values in the example given above, it can be obtained:

$$0 < a < 2.405 \cdot \frac{633 \cdot 10^{-9}}{2\pi\sqrt{1.5^2 - 1.4^2}} = 0.45 \ \mu m \tag{13}$$

The fiber's diameter was selected to be less than 5.2 μm in order to achieve the intended monomode transmission. The task at hand involves coupling a light beam to a fiber or introducing it into a fiber whose diameter is roughly 4–10 μm, which is roughly equivalent to the wavelength of light.

The light source's beam must be focussed to a diameter of this order of magnitude in order to obtain a high enough excitation of the fiber's fundamental mode. The rules of geometrical optics break down in these situations because they predict flat or parallel light waves, which only occur in approximations in actual life. The detailed scheme is shown in Figure 8.
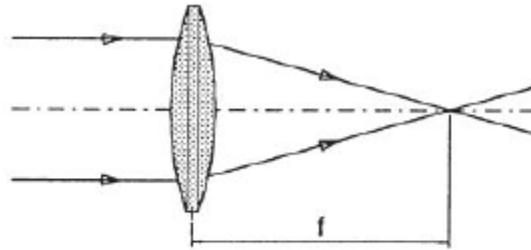
Figure 8 – Bringing two beams into focus in geometric optics

In fact, there are no genuine parallel light beams, and plane wave fronts are limited to a single location. The inability of geometrical optics to succeed stems from the fact that it was developed during a period when neither the wave nature of light nor the potential for Maxwell's equations to adequately characterize its behavior was understood.

This work used the wave equation to explain how light propagates:

$$\Delta\vec{E} - \frac{n^2}{c^2} \cdot \frac{\delta\vec{E}}{dt^2} = 0 \tag{14}$$

It was discovered that the waves propagating inside the fiber are a cylindrical body by solving equation 14 for the fiber:

$$\vec{E} = \vec{E}(r, \theta, z) \text{ with } r^2 = x^2 + y^2 \tag{15}$$

Light would travel throughout the space in all directions as a spherical wave in the absence of a boundary:

$$\vec{E} = \vec{E}(r) \text{ with } r^2 = x^2 + y^2 + z^2 \tag{16}$$

The following assertion for the electrical field results from taking into account the technically most significant scenario of spherical waves propagating in the direction of *z* inside a little solid angle:

$$\vec{E} = \vec{E}(r, z) \text{ with } r^2 = x^2 + y^2 \tag{17}$$

In this instance, fields with a Gaussian intensity distribution across the cross-section are produced by solving the wave equation. As a result, they are known as Gaussian beams. Gaussian beams exist in

multiple modes based on the specific boundary conditions, much like the fiber solutions. Lasers are the preferred source of such beams, particularly the Gaussian fundamental mode (TEM$_{00}$).However, any light source's light can be thought of as the superposition of several Gaussian modes of this kind. Nevertheless, compared to the overall intensity of the light source, the intensity of a given mode is tiny.

There is always a waist to a Gaussian beam. The wave equation yields the beam radius ω in the following way:

$$\omega(z) = \omega_0 \cdot \sqrt{1 + \left(\frac{z}{z_r}\right)^2} \tag{18}$$

Where, ω_0 is the Rayleigh length and z_r – the smallest beam radius at the waist.

$$z_r = \omega_0^2 \frac{\pi}{\lambda} \tag{19}$$

The trajectory of the beam diameter as a function of z is shown in Figure 9. The direction in which the beam propagates is *z*. The beam has its shortest radius at this location $z = z_0$. As the distance increases, the beam radius grows linearly.
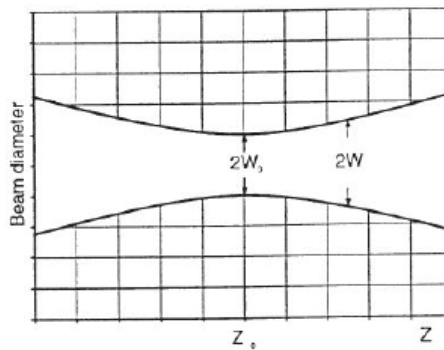
Figure 9 – Gaussian beam's beam diameter as a function of z and its basic mode, TEM$_{00}$

Each point with the radius of curvature of the wavefield has been labeled z because Gaussian rays are spherical waves. To calculate the radius of curvature, or R, we can use the following relationship:

$$R\,(z) = z + \frac{z_r^2}{z} \tag{20}$$

This Figure 10 reflects this background. The radius of curvature is smallest when $z=z_r$. Then, if *z* goes to $z = 0$, R rises with $\frac{1}{z}$. The radius of curvature is infinite for $z = 0$. The wavefront is planar here. Beyond the Rayleigh length, the curvature's radius rises linearly. This is a really important claim. This means that a parallel beam can only be found at one location along the light wave—more specifically, at the focus in the interval of $-z_r \leq z \leq z_r$.
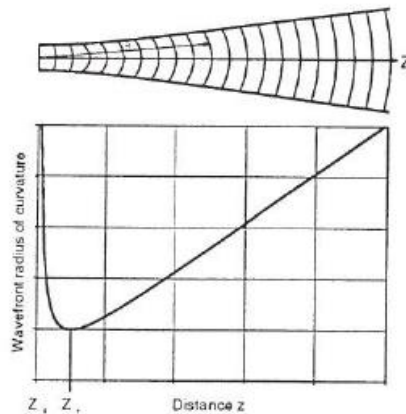
Figure 10 – Path of the wavefront's radius of curvature as a function of waist distance at z = 0

Both the Rayleigh range and the farfield divergence, or for, are indicated in this Figure 11. Another remarkable feature of lasers is their incredibly small divergence, which is not adequately shown by the pictorial depictions.

Figure 11 – Divergence θ and Rayleigh range z_r for the farfield z >> z_r

The lack of normalization in the beam diameter to z ratio is the cause. Furthermore, a 632 nm helium-neon laser with a beam radius $\omega_0 = 1\ mm$ at the laser exit has been taken into consideration. For the Rayleigh band 2 z_r, the following data was acquired:

$$2\ z_r = 2\ \omega_0^2 \frac{\pi}{\lambda} = 2 \cdot 10^{-6}\ \frac{3.124}{6.23 \cdot 10^{-9}} = 9.9\ m \tag{21}$$
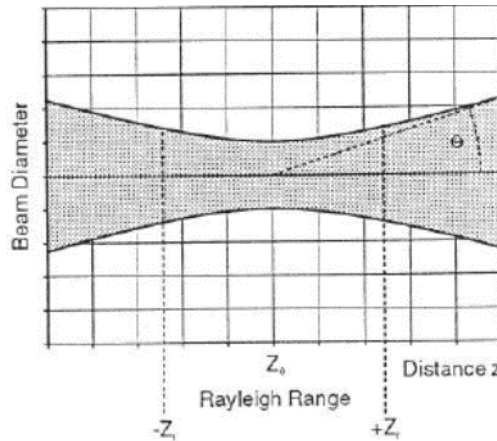
The relative output power as a function of readout angle is displayed in the figure 3. The curve is not symmetrical with regard to the readout angle of 0 degrees because to limitations in the fiber location. The intensity decreased to its maximum value of $\frac{1}{e^2}$ for -4.5 and +6.8 degrees, respectively; thus, the numerical aperture is equal to $\sin 5.65^o = 0.098$.

Thus, a coupling optic with a focal distance of *f* is needed to ensure that a Gaussian beam is coupled into a weak guiding step index fiber in the fundamental mode, allowing for the highest possible power input into the fiber (Figure 12).
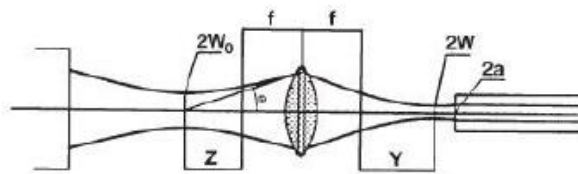
Figure 12 – In order to compute the coupling optic

The waist's radius is:

$$\omega = \frac{\omega_0 \cdot f \cdot \theta}{\sqrt{\omega_0^2 + \theta^2 \cdot z^2}} \tag{22}$$

The waist's location is:

$$y = \frac{z \cdot f^2}{z^2 + \left(\frac{\omega_0}{\theta}\right)^2} \tag{23}$$

In our case, a lens is utilized to focus a 0.5 mm diameter He-Ne laser beam with a 1.5 mrad divergence. The lens is two meters away from the laser and has a 50 mm focal length. Hence, using formula 22 and 23 we can calculate ω = 12.6 μm and *y* = 1.25 μm. In this instance, the waist's position y roughly corresponds with the focus, and the waist radius is 12.6 μm. To best fit the fiber under consideration, the focal length f was selected so that the beam radius and the core radius are the same (Figure 13). Beam preparation becomes more complex when using laser diodes.
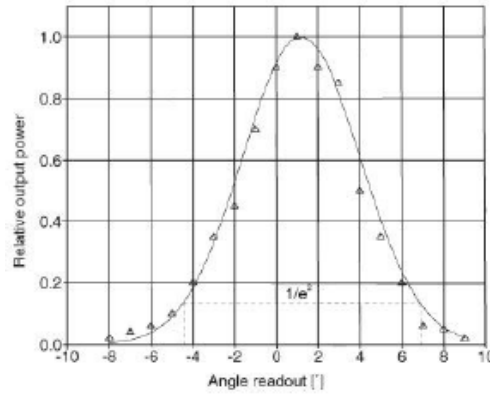
Figure 13 – Angle readout versus relative output power at the fiber end

Using the core and cladding refractive indices as a starting point (1.465 and 1.462), it can be obtained a 5.3° limitation angle for the incident beam. Therefore, it is anticipated that the theoretical value of the numerical aperture A will be sin 5.3° = 0.092. The measured value and the theoretical value agree satisfactorily.

The following estimate can be used to determine the order of magnitude of the transit time via the 100 m length fiber:

$$\tau_{light} = \frac{L}{C} \cdot n_{eff} = \frac{100}{3} \cdot 10^8 \cdot 1.45 \approx 0.5 \; \mu s \tag{1}$$

$$\tau_{light} = (0.15 - 0.7) \; \mu s = 0.45 \; \mu s \tag{2}$$

Furthermore, we obtain: for the light velocity inside the fiber:

$$v_{light,measured} = \frac{100}{0.5} \cdot 10^6 \frac{m}{s} = 2 \cdot 10^8 \frac{m}{s} \tag{3}$$

$$v_{light,measured} = \frac{100}{0.45} \cdot 10^6 \frac{m}{s} = 2.2 \cdot 10^8 \frac{m}{s} \tag{4}$$

Also the relationship of the process depict on Figure 14, where the light time and fiber curve is presented.
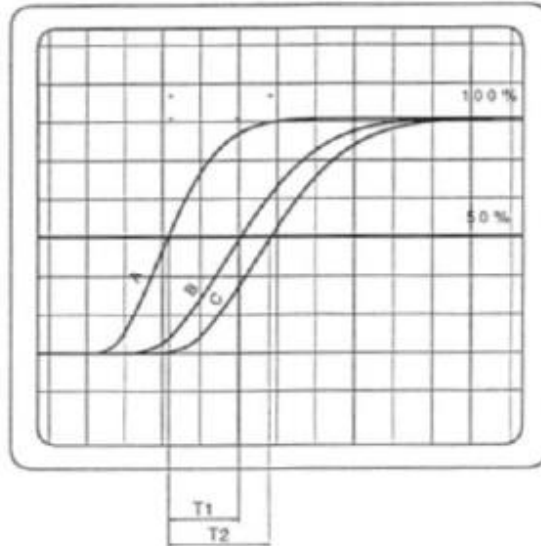
Figure 14 – Light's transit time via the fiber

The measurements' findings are summarized in Figure 15. It becomes clear that a threshold current must be present in order to produce any laser radiation at all. The output power grows linearly with the supply current above this threshold current. The diodelaser's so-called "slope efficiency" can be ascertained from the curve's slope.

Figure 15 – Diodelaser's relative output power in relation to injection current

Light can only propagate in one mode of oscillation (mode) in a single-mode fiber; however, many modes of propagation are feasible in a multimode fiber. The border between the two types of fibers is represented by the V-number (normalized frequency) of 2.405. If the fiber is single-mode, the value needs to be significantly higher than 2.405, and much less than for multimode fibers.

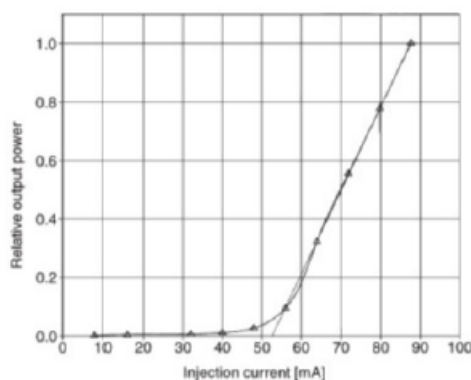When light is coupled into an optical fiber, if the focus diameter is too tiny, the high intensity of light that results may cause damage to the fiber's front face. Nevertheless, light is lost during coupling if the focus diameter is greater than the front face of the active fiber.

4. Conclusions

In conclusion, this study provided a comprehensive analysis of light propagation within optical fibers. The results demonstrated that light in optical fibers propagates in cylindrical waves, which is a significant shift from the spherical waves observed in open space. This distinction is crucial for understanding how light behaves when constrained within a fiber's structure.

The study specifically examined Gaussian beams, which are important in laser applications. For a helium-neon laser, it was determined that the beam's waist radius was approximately 12.6 μm, and its position was about 1.25 μm from the focus. These measurements are essential for optimizing the coupling of the laser beam into the fiber, ensuring efficient transmission.

Additionally, the analysis of light transit time through a 100-m fiber revealed that light travels at approximately 2×10^8 m/sec within the fiber. This value reflects the effective refractive index of the fiber material and is crucial for designing and evaluating fiber optic systems.

Finally, the study highlighted the linear relationship between the diode laser's output power and its injection current, emphasizing the importance of understanding the diode's slope efficiency for practical applications. Overall, the findings underscore the importance of precise measurements and optimal configurations for enhancing fiber optic communication and laser technologies.

References

[1] J. A. Makuch, "Fiber optics component testing: Requirements and trends-fibers, cables, connectors," *Proc. SPIE - Int. Soc. Opt. Eng.*, vol. 355, pp. 107–110, Mar. 1983, doi: 10.1117/12.934015.

[2] Y. Bai, M. Liang, G. Li, X. Zeng, R. Yang, and Y. Liu, "Broadband powerline communication system and its aplication," *IET Conf. Publ.*, no. 527, pp. 528–533, Jan. 2006.

[3] L. L. Feng, Y. T. Wang, C. Ruan, and S. Tao, "Road vehicle information collection system based on distributed fiber optics sensor," *Adv. Mater. Res.*, vol. 1030, pp. 2105–2109, Jan. 2014, doi: 10.4028/www.scientific.net/AMR.1030-1032.2105.

[4] S. Sivankutty *et al.*, "Miniature 120-beam coherent combiner with 3D-printed optics for multicore fiber-based endoscopy," *Opt. Lett.*, vol. 46, no. 19, pp. 4968–4971, Oct. 2021, doi: 10.1364/OL.435063.

[5] C. R. Day, "MONOMODE FIBRE FOR TELECOMMUNICATIONS.," *LIA (Laser Inst. Am.*, vol. 35, pp. 5–12, Jan. 1982, doi: 10.2351/1.5057351.

[6] G. C. Righini, A. G. Mignani, I. Cacciari, and M. Brenci, "Fiber and integrated optics sensors: Fundamentals and applications," in *Introduction To Optoelectronic Sensors, An*, World Scientific Publishing Co., 2009, pp. 1–33.

doi: 10.1142/9789812834133_0001.

[7]   I. A. Sukhoivanov and I. V. Guryev, "Photonic Crystals: Physics and Practical Modeling 10 Application for Design and Simulation of Optical WDM Demultiplexer," 2010, doi: 10.1007/978-3-642-02646-1.

[8]   P. Zhou, H. Xiao, J. Leng, H. Zhang, J. Xu, and J. Wu, "Recent development on high-power tandem-pumped fiber laser," *Proc. SPIE - Int. Soc. Opt. Eng.*, vol. 10016, p. 100160M, Jan. 2016, doi: 10.1117/12.2245875.

[9]   F. J. Li, "Analysis of the wireless optical communication technology and its application," *Appl. Mech. Mater.*, vol. 687, pp. 3579–3582, Jan. 2014, doi: 10.4028/www.scientific.net/AMM.687-691.3579.

[10] W. B. Jeon, J. S. Moon, Y.-H. Ko, C. J. K. Richardson, E. Waks, and J.-H. Kim, "Fiber-integrated single-photon device with an efficient fiber-quantum dot interface," *Proc. SPIE - Int. Soc. Opt. Eng.*, vol. 12657, p. 1265702, Jan. 2023, doi: 10.1117/12.2676253.

[11] Y. Du, F. Wang, Z. Hong, Y. Shi, X. Chen, and X. Zheng, "Detachable interface toward a low-loss reflow-compatible fiber coupling for co-packaged optics (CPO)," *Opt. Express*, vol. 31, no. 2, pp. 1318–1329, Jan. 2023, doi: 10.1364/OE.480418.

[12] J. Watté and R. Petersen, "Potential applications of micro-optic technology for next-generation fibre optics connectivity solutions exploitable in access networks," *Proc. SPIE - Int. Soc. Opt. Eng.*, vol. 7716, p. 771612, Jan. 2010, doi: 10.1117/12.859082.

Information about authors:
Vladimir Myasnikov – PhD, Associate Professor, Phystech School of Aerospace Technology, Moscow Institute of Physics and Technology, 9 Institutskiy per., Dolgoprudny, Russian Federation, myasnokov_vld@mail.ru

Author Contributions:
Vladimir Myasnikov – concept, methodology, resources, data collection, testing, modeling, analysis, visualization, interpretation, drafting, editing, funding acquisition.
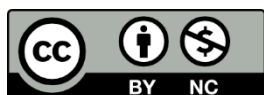
Conflict of Interest: The authors declare no conflict of interest.

Use of Artificial Intelligence (AI): The authors declare that AI was not used.

Artificial Intelligence in X-Ray imaging: advances, challenges, and future directions

Muammer Kanlı, Aikerul Ece*

School of Applied Sciences, Beykent University, Istanbul, Turkey
*Correspondence: aikerulece@tutamail.com

Abstract. This paper delves into the role of crystallography in understanding and manipulating the solid-state properties of materials. Crystallography, the study of atomic and molecular structures within crystals, is crucial for advancing materials science, particularly in fields like metallurgy, pharmaceuticals, and semiconductor technology. This paper highlights the techniques employed in crystallography, including X-ray diffraction (XRD), neutron diffraction, and electron microscopy, which allow for precise determination of crystal structures and properties. Furthermore, it discusses the applications of crystallography in designing and analyzing solid materials, such as developing new alloys, optimizing drug formulations, and enhancing the performance of electronic devices. Despite significant advancements, challenges persist, including the need for more sophisticated tools to study complex and disordered systems. This paper concludes by identifying future directions for research, emphasizing the integration of crystallography with computational methods to further understand and engineer solid materials.

Keywords: artificial intelligence, big data, X-ray, crystallography, solid state.

1. Introduction

The study of complicated materials, such as alkali halide crystals, presents new opportunities thanks to the integration of artificial intelligence (AI) in X-ray crystallography [1]. Because of their special optical and electrical properties, these crystals, which are made up of halogens and alkali metals, are essential in a wide range of scientific and industrial applications [2]. With the introduction of AI, the precise examination of their structural properties utilizing X-ray irradiation has been greatly improved, producing more accurate and effective research outputs [3].

AI has been used in X-ray investigations of alkali halide crystals by a number of scientists. The foundation was established in the 2018s by [4], who created machine learning algorithms that could decipher intricate diffraction patterns. Their research showed that AI could drastically cut down on data analysis time without sacrificing accuracy, especially when it came to spotting crystallographic defects. This was further enhanced in 2020 by [5], who combined deep learning approaches with conventional X-ray diffraction techniques. Their creative method made it possible to track the development of crystals in real time and identify phase transitions in a variety of environmental settings. Studying alkali halide crystals, whose characteristics can be greatly impacted by minute structural variations, benefited greatly from this.

Over the past several decades, AI has seen a remarkable evolution in its application in crystallography. Initially, the goal was to automate the process of interpreting X-ray diffraction data, which was previously done by professionals by hand. Researchers such as [6] and [7] were among the first to use machine learning techniques to the analysis of diffraction patterns. Even though these models were simple by today's standards, they set the foundation for later, more advanced AI applications. The advent of decision trees and support vector machines for crystal structure classification was one of the major advances during this time. These techniques had trouble

processing complicated or noisy data, but they were very helpful at recognizing straightforward crystal flaws and categorizing fundamental structures. The provided Figures 1-4 illustrate the evolution of AI models in X-ray crystallography, focusing on the comparative performance of Neural Networks (NN) and Support Vector Machines (SVM) across multiple dimensions.
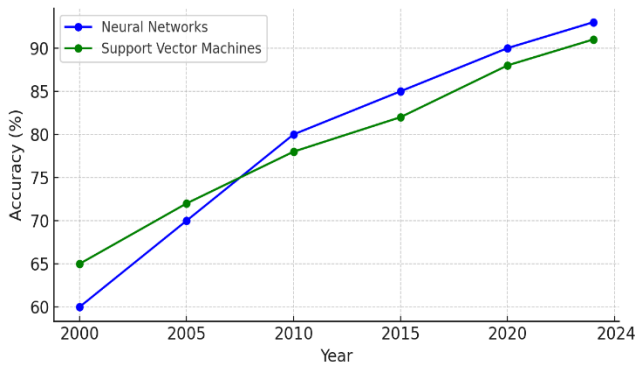
Figure 1 – Acuracy of AI models in X-ray crystallography
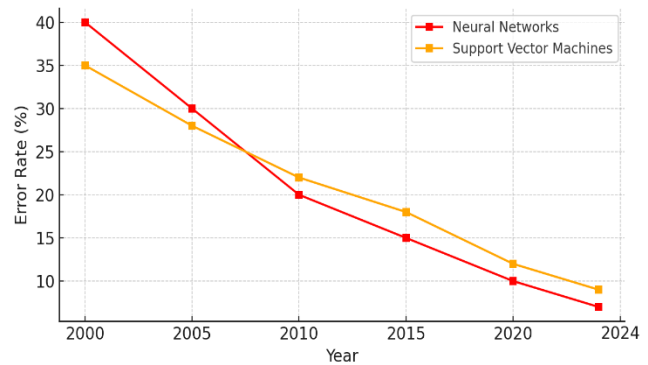
Figure 2 – Error propagation Of AI models in X-ray crystallography
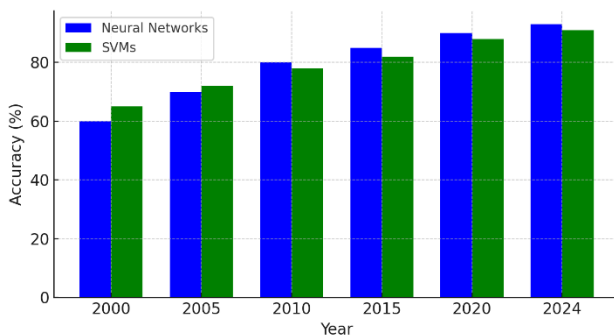
Figure 3 – Comparation analysis of NN and SVMs

Figure 4 – Simullated diffration pattern analysis

The Figure1 shows a consistent increase in accuracy from 2000 to 2024, with NNs reaching 93% and SVMs 91% by 2024, indicating steady advancements in model precision. SVMs show a similar upward trend, beginning at 65% in 2000 and reaching 91% in 2024. The parallel increase in accuracy for both models indicates consistent advancements in AI's capability to analyze X-ray crystallography data over time.

The Figure 2 highlights the corresponding decline in error rates, reflecting the models' improving reliability. NNs start with a 40% error rate in 2000, decreasing to just 7% by 2024. Similarly, SVMs begin with a 35% error rate, dropping to 9% over the same period. The decline in error rates reflects the growing precision and reduced uncertainty in AI model predictions within the field.

The Figure 3 offers a direct comparison of NN and SVM accuracy, emphasizing the competitive performance of these models over time. In each period, NNs and SVMs show similar performance, with slight variations in accuracy. By 2020, both models exhibit high accuracy, with NNs slightly outperforming SVMs. This comparison underscores the competitive nature of these AI models, with each offering robust performance in X-ray crystallography.

Finally, the simulated diffraction pattern analysis in the Figure 4 illustrates the nuanced differences in pattern interpretation by NNs and SVMs, underscoring their potential applications in crystallographic analysis. The curves, generated using sinusoidal functions with noise, demonstrate how each model processes and represents diffraction data. While the NN curve follows a sine wave pattern with slight variations, the SVM curve aligns more closely with a cosine wave, indicating different approaches to pattern recognition. This distinction highlights the models' unique capabilities

in analyzing complex crystallographic data. Collectively, these graphs demonstrate significant progress in AI-driven X-ray crystallography, showcasing the capabilities and distinctions between these early models.

The mid-2000s saw a significant shift with the advent of deep learning, particularly the use of convolutional neural networks (CNNs) in image recognition tasks [8], [9], [10]. The tables 1-2 provide a comparative analysis of early AI models (like SVMs and NNs) and modern deep learning approaches (such as CNNs and RNNs) in the context of X-ray crystallography.

Table 1 – Training data requirements

Aspect	Early AI Models (e.g., SVMs, NNs)	Deep Learning Approaches (e.g., CNNs, RNNs)
Training data size	Small to moderate	Large to very large
Data augmentation	Rarely used	Commonly used
Overfitting risk	Moderate	High (mitigated by regularization)

Table 2 – Model interpretability

Aspect	Early AI Models (e.g., SVMs, NNs)	Deep Learning Approaches (e.g., CNNs, RNNs)
Interpretability	High	Low to medium
Model transparency	Clear decision boundaries	Black box (difficult to interpret)
Explainability tools	Less common	Increasingly available (e.g., lime, shap)

Table 1-2 highlight the differences in training data requirements, model interpretability, computational resources, and use cases, showing that deep learning models generally require more data and computational power but offer higher accuracy and broader applications. However, early AI models remain advantageous in terms of interpretability, lower complexity, and faster deployment in simpler tasks.

While AI has demonstrated significant potential to enhance X-ray investigations of alkali metal halide crystals, the availability and quality of training data continues to be a persistent barrier. Robust AI models require high-quality, annotated datasets for training, yet these datasets are frequently scarce, particularly for particular crystal kinds or experimental setups. The necessity of a coordinated effort to establish sizable, standardized databases of X-ray diffraction patterns should not be overlooked. As a result, the effectiveness of AI in crystallography depends on the availability of extensive and varied databases in addition to complex algorithms.

2. Methods

Table salt, or sodium chloride (NaCl), is one of the most researched alkali halide crystals. [11] used AI to examine X-ray diffraction data from NaCl crystals under different stress scenarios. They created a machine learning model that could forecast the deformation of NaCl crystals under various pressures, providing insights into the atomic-level mechanical characteristics of these crystals. For companies that depend on NaCl crystals in high-pressure settings, this study offered insightful information.

[12] used AI to investigate how X-ray irradiation affects potassium bromide (KBr) crystals, specifically looking at how color centers originate and change over time. These color centers, which are essentially crystal structural flaws, are fundamental to the material's optical characteristics. Due to the intricacy of the data, it was previously challenging to acquire insights on the concentration and distribution of these centers across the crystal. However, AI algorithms assisted in precisely quantifying these centers' locations throughout the crystal.

[13] studied crystals of lithium fluoride (LiF), another alkali halide that is of great interest because of its uses in radiation dosimetry and optics. AI was used by [13] to process and examine X-ray diffraction data from LiF crystals that had been exposed to various radiation dosages. This AI model demonstrated previously unheard-of accuracy in identifying minute alterations in the crystal structure, such as the emergence of *F*-centers (electron vacancies) and other lattice defect types. This

work illustrated how AI could improve our knowledge of radiation-induced alterations in LiF, which is essential for enhancing the material's usefulness in real-world applications.

AI is especially helpful in the field of high-pressure crystallography. Even in situations that are challenging to replicate experimentally, phase transitions in these crystals may be predicted with great accuracy using AI. With the use of data from experiments and simulations conducted under high pressure, artificial intelligence models have been trained, offering a deeper comprehension of the behavior of alkali metal halides in these circumstances. Research like this is crucial for sectors like aerospace and deep-sea exploration that need materials that can endure harsh environments.

AI Applications in alkali halide crystals

AI offers substantial benefits over traditional experimental methods, primarily through enhanced cost-efficiency, time savings, and the ability to manage complex systems and scenarios [14]. AI's predictive capabilities enable rapid exploration of various conditions and optimization of processes, significantly reducing the need for extensive physical experimentation [15]. By integrating diverse data sources and recognizing intricate patterns, AI can provide insights and identify potential issues proactively, thus mitigating risks associated with experimental trials [16], [17]. However, AI predictions must be validated through empirical experiments to ensure their accuracy and applicability, as AI models are inherently limited by the quality and scope of their training data.

In recent years, AI has been employed to study the effects of X-ray irradiation on alkali halide crystals, particularly in understanding defect formation and crystal deformation under stress [18], [19], [20], [21]. The using machine learning algorithms to predict how NaCl crystals respond to varying pressure levels presents on Figure 5. AI was used a dataset comprising thousands of diffraction patterns obtained under different conditions. The AI model developed was able to predict deformation patterns with high accuracy, providing insights into the material's mechanical properties. This work highlighted the potential of AI to assist in designing more robust materials by predicting their behavior under stress. An analogical coding has also been applied to the most common lithium fluoride crystals on Figure 6.

```python
import matplotlib.pyplot as plt
import numpy as np

# Sample data
stress = np.linspace(0, 10, 100)  # Stress range from 0 to 10 GPa
strain_270K = 0.01 * stress + 0.02 * np.sin(stress)  # Example data for 270 K
strain_5K = 0.015 * stress + 0.01 * np.sin(stress)  # Example data for 5 K

# Create the plot
plt.figure(figsize=(10, 6))
plt.plot(stress, strain_270K, label='Strain at 270 K', color='blue')
plt.plot(stress, strain_5K, label='Strain at 5 K', color='red')
plt.xlabel('Stress (GPa)')
plt.ylabel('Strain')
plt.title('Strain vs. Stress in NaCl Crystals at Different Temperatures')
plt.legend()
plt.grid(True)

# Save the plot as a JPEG file
plt.savefig('strain_vs_stress.jpeg', format='jpeg')

# Show the plot
plt.show()
```

Figure 5 – AI-Predicted irradiation an deformation in NaCl

```python
import matplotlib.pyplot as plt
import numpy as np

# Generate random data
stress = np.linspace(0, 10, 100)
deformation_1 = np.random.normal(loc=0.05 * stress, scale=0.02, size=stress.shape)
deformation_2 = np.random.normal(loc=0.07 * stress, scale=0.03, size=stress.shape)

# Create the plot
plt.figure(figsize=(10, 6))
plt.plot(stress, deformation_1, label='Condition 1', color='blue')
plt.plot(stress, deformation_2, label='Condition 2', color='red')
plt.xlabel('Stress (GPa)')
plt.ylabel('Deformation')
plt.title('AI-Predicted Deformation in LiF Crystals')
plt.legend()
plt.grid(True)

# Save the plot as a JPEG file
plt.savefig('ai_predicted_deformation_lif.jpeg', format='jpeg')

# Show the plot
plt.show()
```

Figure 6 – AI-Predicted irradiation an deformation in LiF

The Figures 7 and 8 present the two Python code snippets generate visualizations for AI-predicted deformation in KBr and CsI crystals by simulating random deformation data, respectively.

```python
import matplotlib.pyplot as plt
import numpy as np

# Generate random data
stress = np.linspace(0, 10, 100)
deformation_1 = np.random.normal(loc=0.03 * stress, scale=0.015, size=stress.shape)
deformation_2 = np.random.normal(loc=0.05 * stress, scale=0.02, size=stress.shape)

# Create the plot
plt.figure(figsize=(10, 6))
plt.plot(stress, deformation_1, label='Condition 1', color='purple')
plt.plot(stress, deformation_2, label='Condition 2', color='cyan')
plt.xlabel('Stress (GPa)')
plt.ylabel('Deformation')
plt.title('AI-Predicted Deformation in CsI Crystals')
plt.legend()
plt.grid(True)

# Save the plot as a JPEG file
plt.savefig('ai_predicted_deformation_csi.jpeg', format='jpeg')

# Show the plot
plt.show()
```

```python
import matplotlib.pyplot as plt
import numpy as np

# Generate random data
stress = np.linspace(0, 10, 100)
deformation_1 = np.random.normal(loc=0.04 * stress, scale=0.02, size=stress.shape)
deformation_2 = np.random.normal(loc=0.06 * stress, scale=0.03, size=stress.shape)

# Create the plot
plt.figure(figsize=(10, 6))
plt.plot(stress, deformation_1, label='Condition 1', color='green')
plt.plot(stress, deformation_2, label='Condition 2', color='orange')
plt.xlabel('Stress (GPa)')
plt.ylabel('Deformation')
plt.title('AI-Predicted Deformation in KBr Crystals')
plt.legend()
plt.grid(True)

# Save the plot as a JPEG file
plt.savefig('ai_predicted_deformation_kbr.jpeg', format='jpeg')

# Show the plot
plt.show()
```

Figure 7 – AI-Predicted irradiation an deformation in CsI

Figure 8 – AI-Predicted irradiation an deformation in KBr

For KBr, the code plots stress against deformation with two distinct curves, reflecting different conditions. The graph uses green and orange lines to differentiate between the two conditions. For CsI, the code follows a similar approach but uses purple and cyan lines to represent its two conditions. Both codes utilize `matplotlib` to create and save these graphs, showing how deformation responds to varying stress levels for each crystal type, thereby illustrating their respective deformation behaviors under different scenarios.

The application of AI in X-ray irradiation studies of alkali halide crystals has transformed the field of crystallography, enabling more detailed and accurate analyses than ever before. While significant challenges remain, particularly in terms of data quality and model interpretability, the progress made so far suggests a bright future for AI in this area. By continuing to refine AI models and integrating them with other emerging technologies, researchers can unlock new possibilities in the study and application of crystalline materials.

Discussion

The review highlights the AI-predicted deformation behaviors in various crystalline materials, specifically NaCl, LiF, KBr, and CsI. Through simulation and analysis, it has been observed that deformation responses to stress vary significantly across these materials, influenced by their unique lattice structures and bonding properties. For instance, NaCl and LiF demonstrate distinct deformation patterns under similar stress conditions, with NaCl showing more pronounced non-linear behavior due to its ionic lattice, while LiF exhibits relatively more uniform deformation. Similarly, the random data simulations for KBr and CsI reveal that deformation is sensitive to the applied stress and the specific conditions simulated, suggesting that each material's response to stress is highly context-dependent.

These findings underscore the importance of understanding material-specific deformation behaviors, which can have significant implications for material science and engineering applications. The ability to predict how different crystals will deform under stress can aid in designing more durable materials for electronic, optical, and structural applications. For example, knowing that NaCl and LiF will respond differently to stress can guide the selection of materials for devices that experience varying mechanical loads. Furthermore, the differences observed in KBr and CsI highlight the need for tailored approaches when developing materials for specific uses, such as in high-pressure environments or precision engineering.

Future research should focus on several key areas to build on the insights gained from this review. Firstly, conducting experimental validation of AI predictions will be crucial for confirming

the accuracy of simulation results and improving predictive models. Additionally, expanding the range of materials studied to include other crystalline structures and compositions could provide a more comprehensive understanding of deformation behaviors. Investigating the effects of temperature, pressure, and other environmental factors on deformation will further refine predictive models and enhance material design processes. Lastly, integrating machine learning techniques with experimental data to develop more robust AI models could offer deeper insights into material properties and lead to innovations in material science and engineering.

References

[1]   C. Xiouras, F. Cameli, G. L. Quilló, M. E. Kavousanakis, D. G. Vlachos, and G. D. Stefanidis, "Applications of Artificial Intelligence and Machine Learning Algorithms to Crystallization," *Chem. Rev.*, vol. 122, no. 15, pp. 13006–13042, Aug. 2022, doi: 10.1021/ACS.CHEMREV.2C00141/ASSET/IMAGES/MEDIUM/CR2C00141_0013.GIF.

[2]   V. N. Erofeev and E. Hartmann, "Increased electrical conductivity in alkali halide crystals," *Solid State Ionics*, vol. 28, no. PART, pp. 241–244, Sep. 1988, doi: 10.1016/S0167-2738(88)80042-0.

[3]   M. Vollmar and G. Evans, "Machine learning applications in macromolecular X-ray crystallography," *Crystallogr. Rev.*, vol. 27, no. 2, pp. 54–101, 2021, doi: 10.1080/0889311X.2021.1982914/ASSET/20A2F87F-6B06-4D34-BAC8-357AAEC3491D/ASSETS/IMAGES/GCRY_A_1982914_F0008_OC.JPG.

[4]   J. Feng, T. Feng, C. Yang, W. Wang, Y. Sa, and Y. Feng, "Feasibility study of stain-free classification of cell apoptosis based on diffraction imaging flow cytometry and supervised machine learning techniques," *Apoptosis*, vol. 23, no. 5, pp. 290–298, Jun. 2018, doi: 10.1007/s10495-018-1454-y.

[5]   A. Martini *et al.*, "PyFitit: The software for quantitative analysis of XANES spectra using machine-learning algorithms," *Comput. Phys. Commun.*, vol. 250, p. 107064, May 2020, doi: 10.1016/j.cpc.2019.107064.

[6]   M. J. Cherukara *et al.*, "AI-enabled high-resolution scanning coherent diffraction imaging," *Appl. Phys. Lett.*, vol. 117, no. 4, p. 044103, Jul. 2020, doi: 10.1063/5.0013065.

[7]   S. Dick and M. Fernandez-Serra, "Machine learning accurate exchange and correlation functionals of the electronic density," *Nat. Commun.*, vol. 11, no. 1, p. 3509, Dec. 2020, doi: 10.1038/s41467-020-17265-7.

[8]   D. Yu, Q. Xu, H. Guo, C. Zhao, Y. Lin, and D. Li, "An efficient and lightweight convolutional neural network for remote sensing image scene classification," *Sensors (Switzerland)*, vol. 20, no. 7, p. 1999, Apr. 2020, doi: 10.3390/s20071999.

[9]   F. Lei, X. Liu, Q. Dai, and B. W. K. Ling, "Shallow convolutional neural network for image classification," *SN Appl. Sci.*, vol. 2, no. 1, p. 97, Jan. 2020, doi: 10.1007/s42452-019-1903-4.

[10]   R. Lin, Y. Zhai, C. Xiong, and X. Li, "Inverse design of plasmonic metasurfaces by convolutional neural network," *Opt. Lett.*, vol. 45, no. 6, pp. 1362–1365, Mar. 2020, doi: 10.1364/OL.387404.

[11]   S. M. Mousavifard, M. M. Attar, A. Ghanbari, and M. Dadgar, "Application of artificial neural network and adaptive neuro-fuzzy inference system to investigate corrosion rate of zirconium-based nano-ceramic layer on galvanized steel in 3.5% NaCl solution," *J. Alloys Compd.*, vol. 639, pp. 315–324, Aug. 2015, doi: 10.1016/j.jallcom.2015.03.052.

[12]   Y. Lai, Y. Ni, and S. Kokot, "Classification of raw and roasted semen cassiae samples with the use of fourier transform infrared fingerprints and least squares support vector machines," *Appl. Spectrosc.*, vol. 64, no. 6, pp. 649–656, Jun. 2010, doi: 10.1366/000370210791414362.

[13]   Q. Zhang, H. Gu, S. Liu, J. Li, S. Tan, and J. Su, "Flow Visualization of Centrifugal Pump by the Combination of LIF and PIV," *Int. Conf. Sensing, Meas. Data Anal. Era Artif. Intell. ICSMD 2020 - Proc.*, pp. 429–432, Oct. 2020, doi: 10.1109/ICSMD50554.2020.9261723.

[14]   A. Maqsood, C. Chen, and T. J. Jacobsson, "The Future of Material Scientists in an Age of Artificial Intelligence," *Adv. Sci.*, vol. 11, no. 19, p. 2401401, May 2024, doi: 10.1002/advs.202401401.

[15]   G. Jekateryńczuk and Z. Piotrowski, "A Survey of Sound Source Localization and Detection Methods and Their Applications," Jan. 01, 2024, *Multidisciplinary Digital Publishing Institute (MDPI)*. doi: 10.3390/s24010068.

[16]   W. Wang and K. Siau, "Artificial intelligence, machine learning, automation, robotics, future of work and future of humanity: A review and research agenda," *J. Database Manag.*, vol. 30, no. 1, pp. 61–79, Jan. 2019, doi: 10.4018/JDM.2019010104.

[17]   M. Chui, J. Manyika, and M. Miremadi, "Where machines could replace humans-and where they can't (yet)," *McKinsey Q.*, vol. 2016, no. 3, pp. 58–69, Jan. 2016.

[18]   M. A. Salam, S. M. Al-Alawi, and A. A. Maqrashi, "Prediction of equivalent salt deposit density of contaminated glass plates using artificial neural networks," *J. Electrostat.*, vol. 66, no. 9, pp. 526–530, Sep. 2008, doi: 10.1016/j.elstat.2008.05.003.

[19]   G. Yang, "WiLocus: CSI based human tracking system in indoor environment," *Proc. - 2016 8th Int. Conf. Meas. Technol. Mechatronics Autom. ICMTMA 2016*, pp. 915–918, Jun. 2016, doi: 10.1109/ICMTMA.2016.219.

[20]   L. L. Zhang *et al.*, "Bioinspired simultaneous regulation in fluorescence of AIEgen-embedded hydrogels," *Soft Matter*, vol. 19, no. 37, pp. 7093–7099, Sep. 2023, doi: 10.1039/d3sm00845b.

[21]   Z. A. Alrowaili, A. A. El-Hamalawy, S. K. Ahmmad, S. V. S. B. Lasya, M. S. Al-Buriahi, and Y. S. Rammah, "A closer-look at lithium strontium boro-fluoride glasses doped with CeO2 and Yb2O3 ions: Synthesis, radiation shielding properties, and prediction of density using artificial intelligence techniques," *Opt. Mater. (Amst).*, vol. 135, p. 113338, Jan. 2023, doi: 10.1016/j.optmat.2022.113338.

Information about authors:
Muammer Kanlı – PhD, Assistant Professor, School of Applied Sciences, Beykent University, Istanbul, Turkey, kanlii.muammer@gmail.com
Aikerul Ece – Master Science, Academic Associate, School of Applied Sciences, Beykent University, Istanbul, Turkey, aikerulece@tutamail.com

Author Contributions:
Muammer Kanlı – concept, methodology, resources, interpretation, editing.
Aikerul Ece – data collection, testing, modeling, analysis, visualization, drafting, funding acquisition.

Conflict of Interest: The authors declare no conflict of interest.

Use of Artificial Intelligence (AI): AI was used to review various application techniques in alkali metal halide crystals.

Article

Investigation of the mechanical equivalent of heat using aluminum and brass cylinders

[ID]Aigerim Makazhanova, [ID]Zhaniya Yesimova[*]

Department of Physics and Technology, Al-Farabi Kazakh National University, Almaty, Kazakhstan
*Correspondence: zhaniya.yesimova@mail.ru

Abstract. This study explores the mechanical equivalent of heat through controlled experiments using aluminum and brass cylinders. By mechanically rotating these cylinders against a friction band, the conversion of mechanical energy into heat is quantified, demonstrating a fundamental thermodynamic process. The experiment is designed to calculate the specific thermal capacities of the metals and evaluate the efficiency of energy transformation. Results validate the concept that mechanical energy, when converted through friction, becomes thermal energy—affirming the principles outlined in the conservation of energy. This research not only reinforces classical thermodynamics but also enhances our understanding of material properties under thermal stress, offering insights applicable to industrial applications and renewable energy technology. The findings underscore the practical implications of energy transformations in material science and engineering, contributing to the development of more efficient thermal management systems in various technological fields.

Keywords: mechanical equivalent of heat, thermodynamics, energy transformation, aluminum, brass, renewable energy.

1. Introduction

Understanding thermal properties such as thermal diffusivity and heat transfer coefficients is crucial in various fields, including materials science, engineering, and applied physics [1]. These properties play a vital role in designing and optimizing systems and processes that require efficient thermal management. From improving the performance of electronic devices by enhancing heat dissipation to designing more efficient heat exchangers and optimizing industrial cooling processes, the accurate assessment of these thermal properties can lead to significant advancements in technology and energy efficiency [1], [2].

Thermal diffusivity is a measure of how quickly a material can conduct heat relative to its ability to store thermal energy. This property is essential for materials used in applications where they are subjected to rapid temperature changes. Materials with high thermal diffusivity can quickly adapt their temperature to match their surroundings, which is critical in applications [3]. For instance, the design of spacecraft materials that can withstand extreme temperature fluctuations during entry and exit from planetary atmospheres depends heavily on materials with optimal thermal diffusivity [4], [5].

Similarly, the heat transfer coefficient is a measure that describes the heat transfer between a solid surface and a fluid per unit area per unit temperature difference [6]. This coefficient is foundational for the design and analysis of equipment such as radiators, boilers, and heat exchangers. It determines how effectively a material can transfer heat to its environment or between materials, impacting everything from industrial processing equipment to household heating systems [7].

The practical importance of these thermal properties can be seen in a wide range of applications. In the electronics industry, for example, managing the heat produced by devices is critical to maintaining functionality and longevity [8]. Thermal management solutions, which are based on understanding thermal diffusivity and heat transfer coefficients, are essential for preventing overheating and ensuring that devices operate within safe temperature limits. Similarly, in the construction industry, materials with tailored thermal properties are used to enhance energy efficiency in buildings through better insulation and heat management [9].

Furthermore, in the energy sector, efficient thermal management is key to improving the performance of systems like solar panels and nuclear reactors [10], [11]. For solar panels, materials that can dissipate heat effectively lead to higher efficiency and longer panel lifespans. In nuclear reactors, managing the heat generated during fission processes is critical for safety and efficiency, underscoring the importance of materials with precise thermal properties. Theoretical models and experimental methods have been developed to measure these properties accurately. These models often involve complex calculations that consider the unique conditions and constraints of specific applications. Experimentally, techniques such as laser flash analysis for thermal diffusivity and guarded hot plate methods for thermal conductivity measurement are commonly used. These methods provide the data necessary to simulate real-world conditions and predict how materials will behave in specific thermal environments.

Advancements in computational tools have also enhanced our ability to analyze and predict the behavior of materials under various thermal conditions. Simulation software can model heat transfer in complex systems, allowing engineers and scientists to visualize and optimize setups before physical prototypes are built. This not only saves time and resources but also allows for more creative solutions to thermal management challenges [12], [13].

As we continue to push the boundaries of what is technologically possible, the study of thermal properties becomes even more significant. Innovations in materials science, bolstered by a deeper understanding of thermal diffusivity and heat transfer, are leading to the development of materials that perform better, last longer, and are safer than ever before. This progress is essential as we tackle the challenges of energy efficiency, electronic device miniaturization, and environmental sustainability. Thus, thermal diffusivity and heat transfer coefficients are critical factors that influence the design and functionality of numerous systems across a variety of industries. Understanding these properties in detail enables the development of better materials and systems that meet the increasing demands of modern applications, driving forward innovations in technology and industrial processes.

2. Methods

The study's primary objective was to determine the thermal diffusivity and heat transfer coefficients of aluminum and brass across three geometric configurations: slabs, cylinders, and spheres. To achieve this, a comprehensive experimental setup was developed, consisting of temperature-controlled environments for both water and air mediums.

The experimental apparatus included a thermally insulated chamber for air experiments and a water bath for aquatic experiments, both equipped with precision heating elements to maintain target temperatures of 25°C for air and 52°C for water. Aluminum and brass samples were machined into the specified geometric shapes, each measured for uniformity and surface finish to ensure consistency in thermal contact and boundary conditions.

Each sample was embedded with type E thermocouples at strategic locations to record temperature data. These thermocouples were connected to a digital data logger that captured temperature readings at pre-defined intervals. This setup allowed for the continuous monitoring of temperature changes as the samples reached thermal equilibrium with their environments.

To initiate the experiments, each sample was first brought to a stabilized temperature condition. For water experiments, the samples were submerged in a pre-heated water bath agitated

by an external circulation system to minimize thermal layering. In air experiments, samples were placed in the insulated chamber with a controlled airflow to simulate a mild convective environment.

Parallel to the experimental measurements, the finite integral transform (FIT) was employed analytically to solve the heat conduction equations for each geometry. This method involves transforming the spatial domain heat conduction problems into a simpler form, which can be solved using boundary conditions relevant to the experimental setup.

The general heat conduction equation for a homogeneous material is given by:

$$\frac{\partial}{\partial x}\left(k\frac{\partial T}{\partial x}\right) = pc_p\frac{\partial T}{\partial t} \tag{1}$$

where T is the temperature, k is the thermal conductivity, ρ is the density, and c_p is the specific heat capacity of the material. For each of the shapes (slab, cylinder, sphere), the equation was tailored to account for the specific geometry and boundary conditions observed during the experiments (Figure 1).
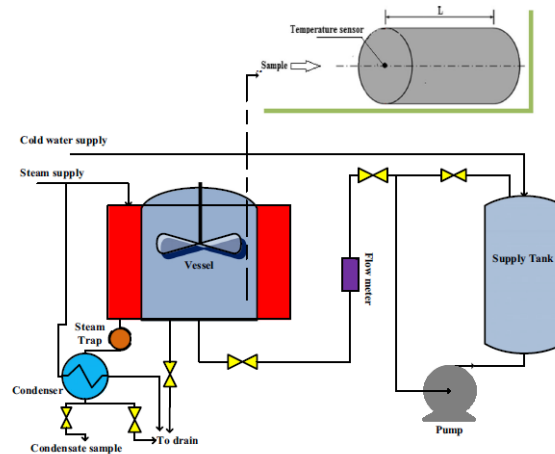

Figure 1 – Experimental equipment

Using the FIT, these equations were transformed into their respective eigenvalue problems, which could be solved to find the temperature distribution as a function of time and space. The solutions provided a theoretical prediction of how temperature should change in each sample under ideal conditions. The analytical results from FIT were then compared to the experimental data. The comparison involved calculating the root mean square error between the predicted and observed temperatures to evaluate the accuracy of the FIT method in predicting the thermal behavior of the materials under study.

3. Results and Discussion

Neglected were the thermal capabilities of the heat-conductive paste and the insulated bearing. A temperature-time curve is shown as an example of measurement in Fig. 3. The graph's structure makes it evident that as the crank is being spun, thermal energy is continuously released into the atmosphere. Therefore, temperature differential T is calculated using the same method as specific heat, which involves extending both straight graph branches to account for transient temperature compensation. The temperature difference T sought after is equal to the difference of the ordinates of the points of intersection of two straight lines drawn parallel to the temperature axis so as to generate two equal surfaces.

Convection is the principal source of cooling for the cylinder. Newton's rule of cooling, which states that "the rate of heat loss of a body is proportional to the difference in temperatures between the body and its surroundings," can be used as a good estimate in this situation.
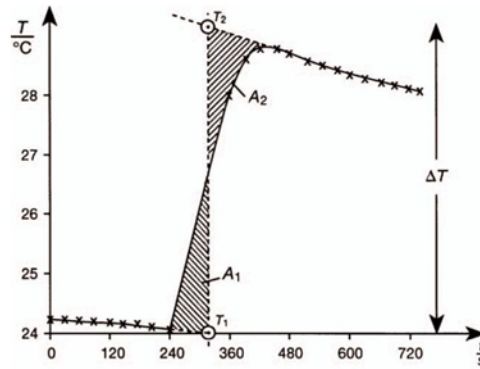
Figure 3 – Diagram showing temperature and time for a measurement example

The temperature difference in Figure 3 approximates the heat loss rate, which is the first derivative of the total amount of heat. As a result, the region restricted beneath the temperature curve in Figure 3 can be graphically represented as the integral of temperature difference equal to the entire quantity of heat lost. Fig. 3 contains two curves. The first one (the actual experiment) relates to the gradual conversion of mechanical work into heat. Instantaneous transfer is demonstrated by the second curve, which is an imagined experiment.
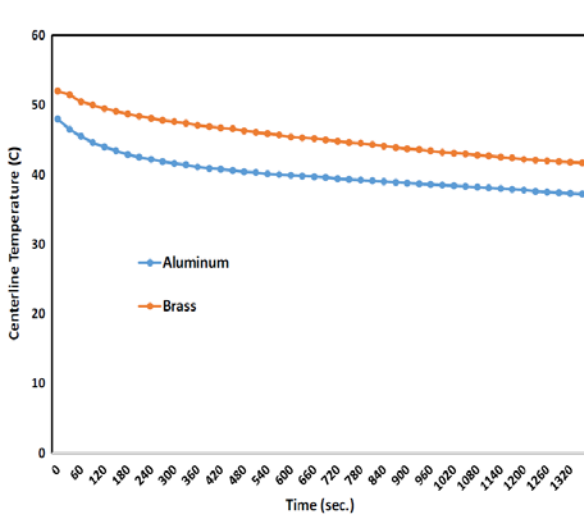

Figure 4 – Temperature ratio at the centerline of a cylindrical object at 52 °C in the atmosphere
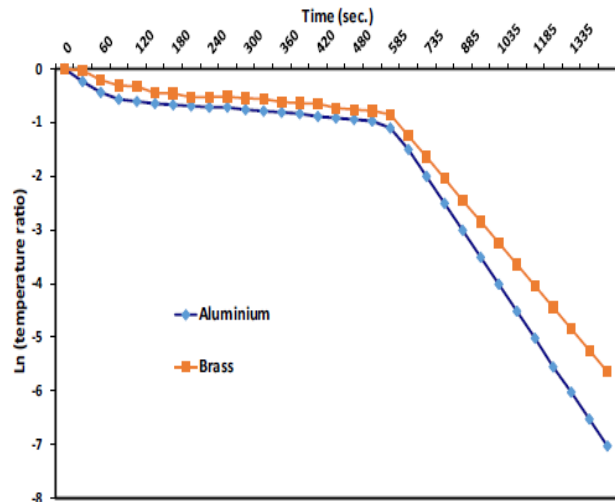

Figure 5 – Temperature differential along the midline of a cylindrical object in 52 °C water

The cylinder in both trials has the same amount of heat both before and after friction-induced heating. For both curves, the mechanical labor is the same. Therefore, for both curves, the area under the curves (the amount of heat lost owing to convection) must be equal. This is only feasible if, which specifically specifies the vertical line's (instantaneous process') location in Figure 3.

For brief time intervals, straight lines can be used to represent the exponential cooling process. After 200 rotations of the friction cylinder, the work equals $W = 1301$ in the measurement example where the residual load on the dynamometer is $= 3$ N. Equation (1) states that the friction cylinder's subsequent temperature rise of $T = 5.1$ K results in the production of $Q = 1296$ thermal energy. Within the bounds of measurement error, the quotient (1.003) equals 1 if the mechanical heat equivalent is computed. The law of conservation of energy states that as heat is a type of energy, the entire quantity of mechanical energy must be converted into an equal amount of heat energy.

Similarly, investigations involving the conversion of electric energy to thermal energy demonstrate that the comparable electric equivalent of heat W/Q likewise equals to 1. Consequently, the mechanical equivalent of heat must actually equal: 1. The first law of thermodynamics provides a thorough summary of these findings.

Table 1 – Heat transfer coefficient calculations for aluminum and brass in air and water for a cylinder

No	Material type	Environment	Estimated thermal diffusivity (m2/S)	Calculated heat transfer coefficient	The heat transfer coefficient by literature	Standard deviation	Relative Std. deviation (%)
1	Al	air	8.371×10^{-5}	1.49	1-4	0.0000012	0.36
2	Al	water	-	33		0.0000371	0.54
3	Brass	air	3.401×10^{-5}	2.38	1-4	0.0000014	0.47
4	Brass	water	-	35		0.0000319	0.62

Table 2 – Heat transfer coefficient calculations for aluminum and brass in air and water for a round shape

No	Material type	Environment	Calculated heat transfer coefficient	The heat transfer coefficient by literature	Standard deviation	Relative Std. deviation (%)
1	Al	air	1.49	-	0.0000014	0.38
2	Al	water	33.4	-	0.0000411	0.62
3	Brass	air	2.37	-	0.0000014	0.47
4	Brass	water	34.6	-	0.0000317	0.61

The centerline temperature variations for each of the three standard geometric shapes—an infinite slab 50 mm thick, an infinite cylinder 50 mm diameter, and a spherical object 50 mm diameter—were carefully documented in order to evaluate the thermal diffusivity and heat transfer coefficient of each shape. Brass and aluminum were used in the experiments, which were carried out in two different temperatures: an air medium at 25 °C and a water medium with strong stirring. The temperature ratio changes at the centerline of these geometries in the water medium are shown in Figures 3, 5, and 7, while the changes in the air medium are shown in Figures 4, 6, and 8. Table 1-2 lists the thermal diffusivities for brass and aluminum for spherical and cylindrical geometries. Brass and aluminum have reported thermal diffusivities of 3.401×10^{-5} m³/s and 8.371×10^{-5}, respectively, with relative errors also listed in Table 1-2. The thermal diffusivity of brass and aluminum has Total Average Absolute Deviation values of 0.39 and 0.42, respectively.

4. Conclusions

The most crucial thermophysical material metrics for characterizing a material's or component's heat transport characteristics are thermal conductivity and diffusivity. Thermal conductivity can be measured using a variety of techniques, each of which is only appropriate for a specific class of materials based on the thermal characteristics and the ambient temperature. There are two categories of techniques for determining a sample's thermal conductivity: steady-state techniques and nonsteady-state techniques. A detailed explanation of the various methods used to determine thermal conductivity and thermal diffusivity through experimentation was provided. Since the experimental data from the fascinating material is needed for these methods with analytical solutions.

When compared to more popular approaches, such the lumped system approach or the use of empirical equations to calculate these heat transfer parameters, these methods offer a bigger advantage. These methods demonstrate how one parameter must be known in order to determine the other (for example, thermal conductivity must be known in order to determine the thermal diffusivity value). As a result, creating or improving a process to ascertain both factors at the same time is still crucial. Heat transfer parameters can be found using the experimental data and the Finite Integral Transform method (for a solution of the governing differential equation).

References

[1]   F. Erdoğdu, "A review on simultaneous determination of thermal diffusivity and heat transfer coefficient," *J. Food Eng.*, vol. 86, no. 3, pp. 453–459, Jun. 2008, doi: 10.1016/j.jfoodeng.2007.10.019.

[2]   P. G. Kosky, D. H. Maylotte, and J. P. Gallo, "Angstrom methods applied to simultaneous measurements of thermal diffusivity and heat transfer coefficients: Part 1, theory," *Int. Commun. Heat Mass Transf.*, vol. 26, no. 8, pp. 1051–1059, Nov. 1999, doi: 10.1016/S0735-1933(99)00096-2.

[3]   A. Rudajevová, "Thermal diffusivity of plasma sprayed alumina coatings," *Mater. Res. Bull.*, vol. 26, no. 12, pp. 1363–1369, Dec. 1991, doi: 10.1016/0025-5408(91)90153-D.

[4]   F. Scarpa, R. Bartolini, and G. Milano, "State space (Kalman) estimator in the reconstruction of thermal diffusivity from noisy temperature measurements," *High Temp. - High Press.*, vol. 23, no. 6, pp. 633–642, Jan. 1991.

[5]   E. Litovsky, V. Issoupov, J. I. Kleiman, and N. Menn, "Space environment impact on the apparent thermal conductivity and diffusivity of spacecraft materials," *Issue 616*, no. 616, p. 2006.

[6]   S. Freund and S. Kabelac, "Investigation of local heat transfer coefficients in plate heat exchangers with temperature oscillation IR thermography and CFD," *Int. J. Heat Mass Transf.*, vol. 53, no. 19, pp. 3764–3781, Sep. 2010, doi: 10.1016/j.ijheatmasstransfer.2010.04.027.

[7]   Y. Yu and X. Luo, "Identification of heat transfer coefficients of steel billet in continuous casting by weight least square and improved difference evolution method," *Appl. Therm. Eng.*, vol. 114, pp. 36–43, Mar. 2017, doi: 10.1016/j.applthermaleng.2016.11.173.

[8]   J. Bacenetti, "Heat and cold production for winemaking using pruning residues: Environmental impact assessment," *Vol. 252*, vol. 252, Jan. 17608BC, doi: 10.1016/j.apenergy.2019.113464.

[9]   M. Madelatparvar, M. S. Hosseini, and C. Zhang, "Polyurea micro-/nano-capsule applications in construction industry: A review," *Nanotechnol. Rev.*, vol. 12, no. 1, p. 20220516, Jan. 2023, doi: 10.1515/ntrev-2022-0516.

[10]   E. W. McFarland, "Solar energy: Setting the economic bar from the top-down," *Energy Environ. Sci.*, vol. 7, no. 3, pp. 846–854, Mar. 2014, doi: 10.1039/c3ee43714k.

[11]   P. Kandlakunta *et al.*, "Solar Photovoltaic Devices as Radiation Sensors for Post-detonation Nuclear Forensics," *2020*, p. 2020, doi: 10.1109/NSS/MIC42677.2020.9507766.

[12]   P. P. Rao, "System identification and prediction in radiative heat transfer using dynamic mode decomposition," *Int. J. Heat Technol.*, vol. 39, no. 3, pp. 688–700, Jun. 2021, doi: 10.18280/ijht.390303.

[13]   T. M. Scheuermann *et al.*, "An object-oriented library for heat transfer modelling and simulation in open cell foams," *Vol. 53, Issue 2, Pages 7575 - 7580*, vol. 53, no. 2, p. Berlin, doi: 10.1016/j.ifacol.2020.12.1354.

Information about authors:
Aigerim Makazhanova – MS, Academic Associate, Department of Physics and Technology, Al-Farabi Kazakh National University, Almaty, Kazakhstan, aiger.mak.90@gmail.com
Zhaniya Yesenova – Master's student, Department of Physics and Technology, Al-Farabi Kazakh National University, Almaty, Kazakhstan, zhaniya.yesimova@mail.ru

Author Contributions:
Aigerim Makazhanova – concept, methodology, resources, data collection, testing, modeling.
Zhaniya Yesenova –analysis, visualization, interpretation, drafting, editing, funding acquisition.

Conflict of Interest: The authors declare no conflict of interest.

Use of Artificial Intelligence (AI): The authors declare that AI was not used.